ACCSCIENCE PUBLISHING

International Journal of Bioprinting

RESEARCH ARTICLE

Three-dimensional bioprinting of gelatin methacryloyl hydrogel with a tri-layered vascularized architecture for full-thickness skin regeneration

Yichen Luo[1], Dan Li[2], Cai Lin[3], Xue Zhou[1], Jien Ma[4]*, and Bin Zhang[1]*

[1]State Key Laboratory of Fluid Power & Mechatronic Systems, School of Mechanical Engineering, Zhejiang University, Hangzhou, Zhejiang, China

[2]Department of Electro-Hydraulic Technology and Equipment Research Center, Binhai Industrial Technology Research Institute of Zhejiang University, Tianjin, China

[3]Department of Burn, The First Affiliated Hospital of Wenzhou Medical University, Wenzhou, Zhejiang, China

[4]Department of Electrical Engineering, College of Electrical Engineering, Zhejiang University, Hangzhou, Zhejiang, China

(This article belongs to the *Special Issue: Advances in 3D Bioprinting*)

Abstract

The skin is the largest organ of the human body and is the primary barrier against external stressors. However, in cases of severe skin damage or pathological conditions, the body's natural physiological repair mechanisms are often insufficient to support effective skin tissue repair and regeneration. Bioprinting, a form of three-dimensional (3D) printing technology, utilizes various biomaterials and cells to construct complex 3D structures, offering the potential to overcome the limitations of conventional tissue-engineered skin and to develop functional skin substitutes. In this study, we developed a 3D bioprinter with excellent printing performance to fabricate vascularized skin substitutes. Through methacrylic anhydride-mediated modification of gelatin, we synthesized gelatin methacryloyl (GelMA) with varying degrees of substitution. The resulting GelMA hydrogel exhibited excellent mechanical properties, swelling ratio, porosity, and rheological properties. To create a hydrogel-multicellular composite bio-ink, we adjusted the concentration of the GelMA solution and co-cultured human immortalized epidermal cells, human foreskin fibroblasts, and human umbilical vein endothelial cells to optimize biological function. Importantly, by fine-tuning the printing parameters, the 3D extrusion-printed lines successfully fused into a continuous membrane, enhancing interlayer bonding and mechanical integrity. This process enabled the construction of a vascularized skin substitute with distinct reticular and papillary layers. In addition, the 3D-printed vascularized skin was implanted into skin defect models established in *BALB/c* nude mice and New Zealand rabbits to investigate its regenerative capabilities. These findings hold significant implications for the utilization of 3D-printed vascularized skin for improving skin injury repair, thereby advancing the field of skin tissue engineering.

Keywords: Three-dimensional bioprinting; Gelatin methacryloyl; Skin injury; Vascularized skin

***Corresponding authors:**
Bin Zhang
(zbzju@zju.edu.cn)

Jien Ma
(majien@zju.edu.cn)

Citation: Luo Y, Li D, Lin C, Zhou X, Ma J, Zhang B. Three-dimensional bioprinting of gelatin methacryloyl hydrogel with a tri-layered vascularized architecture for full-thickness skin regeneration. *Int J Bioprint*. 2025;11(4):328-349. doi: 10.36922/IJB025090069

Received: February 26, 2025
1st revised: March 24, 2025
2nd revised: April 14, 2025
Accepted: April 15, 2025
Published online: April 16, 2025

1. Introduction

The skin is the largest organ of the human body, comprising the epidermis, dermis, and subcutaneous tissue arranged in distinct layers. It serves as a critical protective barrier. However, conditions such as burns, trauma, ulcers, and cancer can cause varying degrees of skin damage. For large-area skin defects, skin grafting is often required. The most common clinical grafting techniques are split-thickness and full-thickness skin grafts. Since these methods use autologous skin, they carry minimal risk of immune rejection and generally result in favorable recovery outcomes. However, their application is limited by the availability of donor sites. Therefore, developing a straightforward method to fabricate skin substitutes remains highly desirable.

Three-dimensional (3D) bioprinting enables the precise spatial organization of biomaterials and cells to create functional skin substitutes. This technology deposits bio-inks layer-by-layer to recreate native tissue microenvironments. Currently, 3D bioprinting skin substitute methods include inkjet printing, laser printing, photopolymerization printing, and extrusion printing. Inkjet printing, the earliest technology applied in bioprinting, was used by Lee *et al.*[1] from Konkuk University to construct dermal and epidermal skin substitutes by printing cell-containing collagen/fibrinogen. Michael *et al.*[2] fabricated a bilayer skin substitute using laser technology, employing a tissue-engineered skin scaffold as a base, on which they printed layers of dermal fibroblasts and keratinocytes and applied it to treat skin defects in mice. However, skin substitutes constructed using inkjet printing often suffer from poor mechanical strength, while the metal absorption substrate used in laser printing may release metal particles under high-energy laser exposure, potentially contaminating the cells. Photopolymerization printing materials must possess photosensitive properties, which limits their application in constructing skin substitutes. Extrusion printing, which uses air pressure or screw extrusion to push bio-ink through a nozzle, deposits it on the platform according to the preset path to form the printed structure.[3–6] Compared to other printing methods, it is highly suitable for constructing complex biological tissues and organs with multiple cells and materials. It is widely applied in research on printing skin substitutes.

Bio-ink selection is critical for skin bioprinting, requiring optimal printability, biocompatibility, and certain mechanical properties.[7–9] Both natural and synthetic biopolymers have been explored for 3D-printed skin constructs. Common natural biopolymers include gelatin, collagen, hyaluronic acid, cellulose, alginate, chitosan, and decellularized extracellular matrix derived from animal tissues. Synthetic biopolymers include polyethylene glycol,[10] polyethylene glycol,[11] polylactic acid,[12] polycaprolactone,[13] and poly(lactic-co-glycolic acid).[14] Gelatin methacrylate (GelMA) is a modified gelatin-based hydrogel renowned for its superior photocrosslinking properties. The hydrogel contains matrix metalloproteinases and arginine-glycine-aspartic acid sequences, facilitating cell migration, adhesion, proliferation, and differentiation. GelMA boasts a range of advantageous properties, including excellent thermosensitivity, outstanding photocrosslinking capability, non-toxicity, and good biocompatibility. Zhao *et al.*[15] reconstructed a multilayer epidermis, which benefited from the sufficient hardness of high-concentration GelMA (20% w/v). According to the research of Xu *et al.*,[16] low-concentration GelMA with large pores, although having weak material stiffness, is beneficial to the growth and proliferation of fibroblasts. This concentration-dependent behavior enables precise layering of skin substitutes.

Currently, research on skin substitutes focuses on constructing skin models with appendage structures, including blood vessels,[17,18] nerves,[19,20] and hair follicles,[21-23] to enhance graft survival and enable more physiologically relevant drug testing. Various bioprinting strategies have been explored to create such complex structures. For instance, Motter *et al.*[24] developed a bilayered skin substitute using collagen-based bio-inks containing human follicle dermal papilla cells, fibroblasts, and keratinocytes, which formed follicular structures during culture. Researchers from Tsinghua University utilized GelMA[25] and Matrigel[26] as matrix hydrogels to encapsulate epidermal stem cells and skin precursor-derived cells obtained from mice. The newly formed skin at the site of skin defects in mice exhibited the formation of vascular and follicular appendages, among other structures. Dai *et al.*[27] from the National Taiwan University utilized a composite hydrogel mixed with polyurea and gelatin as the dermal ink, loaded with human fibroblasts and endothelial progenitor cells, and used keratinocytes as the epidermal ink to construct a pre-vascularized bilayer skin substitute. This was then implanted into a nude mouse defect model to validate its repair and angiogenesis effects. Ma *et al.*[28] employed a composite hydrogel scaffold made of strontium silicate, cold-set gelatin, sodium alginate (SA), and methylcellulose, on which vascular endothelial cells and fibroblasts were deposited to form a pre-vascularized skin (VS) scaffold. *In vivo* experiments demonstrated that this skin substitute actively promoted vascular formation. Barros *et al.*[29] used a mixture of GelMA and SA hydrogels to encapsulate vascular endothelial cells, and GelMA hydrogel to encapsulate fibroblasts, constructing the pre-vascularized and dermal layers layer-by-layer. On the surface of the dermal layer, a multi-layered keratinocyte layer was rapidly formed by

repeatedly dropping a low-concentration gelatin solution containing keratinocytes, ultimately resulting in a pre-vascularized multi-layered skin substitute. Despite these advances, significant challenges remain. Many studies primarily assess endothelial cell viability without fully characterizing *in vitro* microvascular network formation or functionality. Effective vascularization is critical for nutrient delivery, oxygenation, and tissue integration, yet current methods often fail to recapitulate the hierarchical vascular networks found in native skin.

Therefore, this study aimed to construct a multi-layered skin substitute with a vascularized structure. First, we modified gelatin with methacrylic anhydride to obtain GelMA hydrogels with different degrees of functionalization. We then characterized the physicochemical properties, printability, and biocompatibility of the GelMA. By adjusting the concentration of GelMA solutions and optimizing the culture parameters for epidermal cells, dermal cells, and vascular endothelial cells, we prepared a hydrogel-based, cell-compatible composite ink for VS. Using 3D extrusion printing technology, we constructed a stable *in vitro* dermal VS substitute. Additionally, the 3D-printed VS was implanted into skin defect models to further investigate its reparative effects on damaged tissue. We believe this study provides a promising skin substitute for clinical applications and offers valuable insights for future research.

2. Methods

2.1. Three-dimensional bioprinting equipment

We independently developed a 3D bioprinting device. The device comprises a temperature control module, a motion module, a material supply module, and a control module. The constructed 3D bioprinting device is shown in Figure 1,

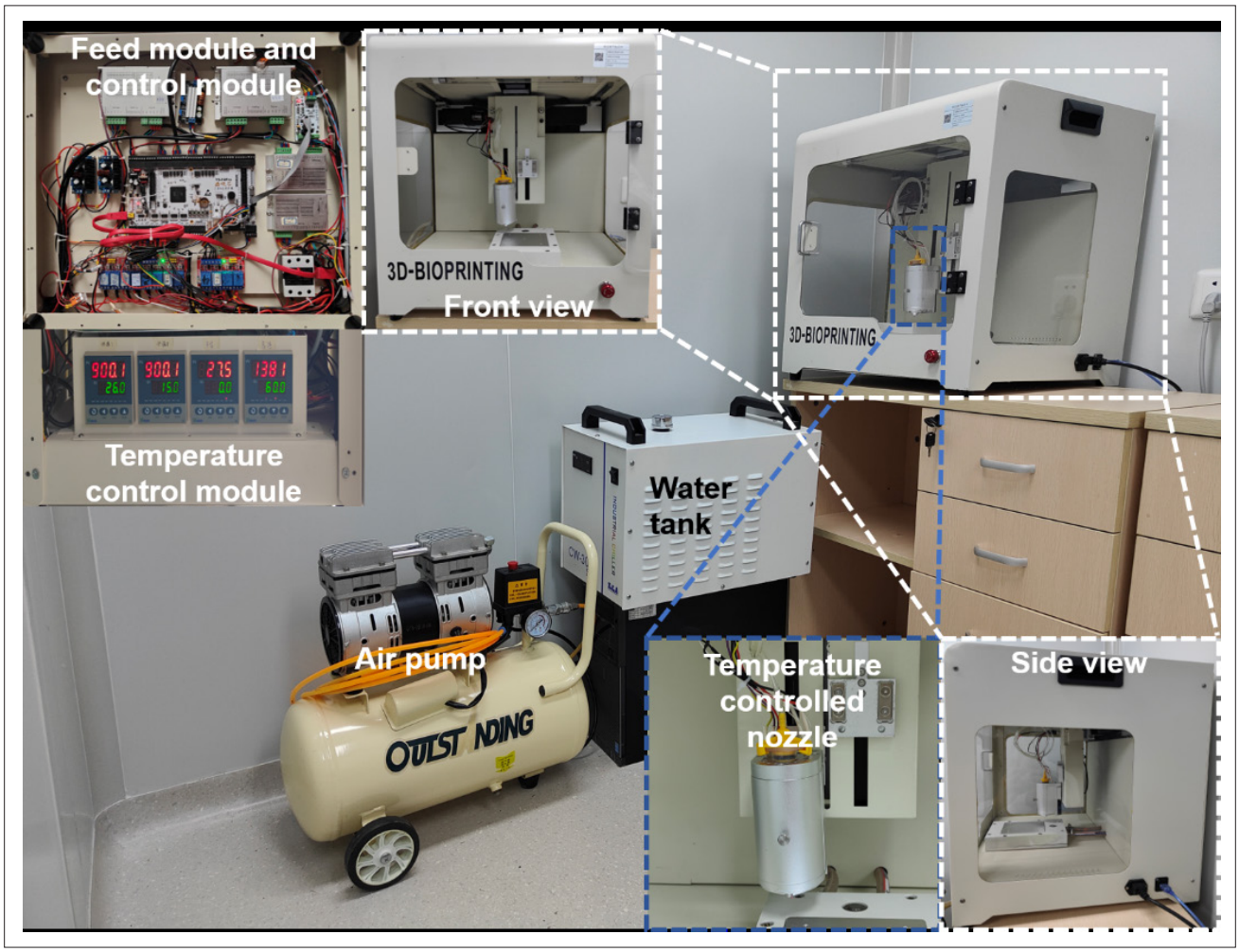

Figure 1. Overall assembly diagram of the printing equipment system.

in which the constant temperature controller of the feeding and control module and the temperature control module are distributed inside the chassis. The overall size of the printing device is 450 mm × 450 mm × 500 mm, and it can be used as a desktop-level printer. The software-controlled host computer system is programmed with LabVIEW software, and the lower computer is developed with an STM32F407 single-chip microcomputer (LabVIEW 2020, STM32F407 single-chip microcomputer 5.0+).

2.2. Print device test

Vasovascular skin substitute printing involves multi-ink printing. The repetitive positioning accuracy of the printing nozzle has a great influence on the final forming quality.[30,31] This equipment was designed with a reset sensor button in the *z*-axis direction, which was used to locate the knife each time the nozzle was replaced. This paper defines the repetitive positioning accuracy of nozzle replacement as D (**Equation I**). The *x*-axis deviation is ΔX, the *y*-axis deviation is ΔY, and n is the number of random tests.

$$D = \frac{\sum_{i=1}^{n}\sqrt{\Delta X^2+\Delta Y^2}\times 100\%}{n} \quad \text{(I)}$$

The SA/gelatin composite hydrogel was printed in the shape of a five-pointed star and an ear using a single-nozzle printing method, and the parameters selected are shown in Table 1. Multi-ink simulation printing of a 10% (w/v) GelMA hydrogel mixed with different ink colors was used to print a multi-layer skin.

2.3. Synthesis of gelatin methacrylate

In this study, GelMA was synthesized using an improved process. Briefly, 10 g of type A gelatin (Sigma, Germany) was dissolved in 100 mL of 0.25 M sodium bicarbonate (Macklin, China) buffer solution with a pH of 8.5. Methacrylic anhydride (Sigma, Germany) was added, and the mixture was stirred at 50°C for 2 h. After that, it was centrifuged at 4000 rpm for 10 min to remove the precipitate, and the clear supernatant extract was retained. Then, 200 mL of warm sodium bicarbonate solution was added to adjust the pH to 7.4, and the mixture was stirred at 40°C for 0.5 h. The solution after the reaction was put into a dialysis bag with a molecular weight cutoff of 12–14 kDa and dialyzed in pure water at 40°C for 1 week. The solution was filtered through a 0.22 μm filter membrane and freeze-dried for 3 days, resulting in white porous foamy GelMA, which was stored at –80°C. The synthesized GelMA was verified using proton nuclear magnetic resonance (JEOL, Japan), and the formula is presented in **Equation (II)**.

$$DoF = \left(1-\frac{lysine\ methylene\ pronton\ of\ GelMA}{lysine\ methylene\ pronton\ of\ Gelatin}\right)\times 100\% \quad \text{(II)}$$

2.4. Characterization of gelatin methacrylate

The GelMA was dissolved in phosphate buffer saline (PBS) containing 0.5% (w/v) lithium phenyl-2,4,6-trimethylbenzoylphosphinate and filtered using a 0.22-μm filter membrane. Finally, GelMA at concentrations of 5% (w/v), 10% (w/v), 15% (w/v), and 20% (w/v) was obtained as the bio-ink, and their mechanical modulus, swelling ratios, porosity, and rheological properties were measured, respectively.

The GelMA mechanical modulus was tested using a dynamic thermomechanical analyzer (DMATAQ800, TA Instruments, United States), employing uniaxial tensile and compression methods. In the tensile test, the sample was made into a dumbbell shape with a thickness of 4 mm, and the cross-sectional area of the middle section of the dumbbell was 16 mm^2. A pre-stress of 0.01 N was applied, and the dumbbell sample was clamped at a strain rate of 0.1 N/min from 0.01 to 10 N until the sample was crushed. In the compression test, the sample was shaped cylindrically with a diameter of 12 mm and a thickness of 2 mm, and the GelMA cylinder was compressed at a strain rate of 10 N/min in the range of 0.01–18 N until the sample was crushed. The swelling sample resulted in a cylindrical hydrogel with a diameter of 12 mm and a thickness of 2 mm. After the sample was prepared, it was immediately weighed as W_0 and then transferred to a 12-well plate of PBS and stored in a 37°C and 5% carbon dioxide incubator for 24 h. After taking it out, the surface water was absorbed using dust-free paper, and the wet weight W_d was measured. The formula is as follows in **Equation (III)**.

$$SR = \frac{W_d - W_0}{W_0}\times 100\% \quad \text{(III)}$$

The GelMA samples were freeze-dried and split into two halves to expose the cross-section, followed by coating

Table 1. Model printing parameters

Structure	Needle model	Extrusion pressure	Print speed	Print temperature	Print layers
Five-pointed star model	30 G	0.7 bar	2 mm/s	27°C	10
Human ear model	30 G	0.9 bar	4 mm/s	27°C	81

with gold-palladium. The morphology of samples was observed using scanning electron microscopy (SU-8010, Hitachi, Japan), with a working distance of 9 mm and an accelerating voltage of 15 kV, and analyzed using ImageJ (**ImageJ2 2.14.0**). The rheological properties of GelMA hydrogel samples were measured using an MCR302 rotational rheometer (Anton Paar, Austria). At a fixed frequency of 1 Hz, the storage modulus (G') and loss modulus (G'') were measured as the temperature decreased from 40 to 4°C at a rate of 5°C/min. To assess the effect of temperature on viscosity, measurements were taken at a constant shear rate of 50/s within the same temperature range. At 25°C, the relationship between the shear rate and viscosity was observed within the 0–500/s range.

2.5. Cell culture

Human umbilical vein endothelial cells (HUVECs), human foreskin fibroblasts (HFF), and human immortalized epidermal cells (HaCaT) (SUNNCELL, China) were cultured in Dulbecco's modified Eagle Medium/Nutrient Mixture F-12 supplemented with 15% fetal bovine serum and 1% penicillin/streptomycin at 37°C and 5% carbon dioxide. HUVECs and HFF were routinely passaged onto a tissue culture flask and were discarded after 8 and 12 passages, respectively, to ensure the representation of key characteristics. Culture media was changed every 2 days, and cells were sub-cultured upon reaching 80–90% confluency.

2.6. Printability and biocompatibility

According to the gel point test results of the GelMA hydrogel, printing tests were carried out for GelMA with concentrations of 5%, 10%, 15%, and 20% (w/v) within the temperature ranges of 13–17, 15–19, 17–21, and 20–24°C, respectively. The printing speed was 6 mm/s, the pressure was 0.1–1.2 bar, the needle type was 30 G, and a two-layer grid structure was printed. A smaller needle diameter typically improves printing resolution but may compromise cell viability due to higher shear stress. Therefore, we selected a 30 G needle to balance resolution and cell viability.

For cell-loaded printing, 10% (w/v) GelMA loaded with HFF cells (1×10^6/mL) were used to print the grid and film structures. During printing, the nozzle temperature was controlled at 18°C, and the low-temperature platform temperature was controlled at 8°C; the needle type selected was 30 G. After printing, the samples were irradiated with 405 nm blue light for 60 s, followed by the addition of culture medium and incubation. Both samples were dyed with LIVE/DEAD® Viability/Cytotoxicity Kit (Thermo Fisher, United States) within an hour after printing and on the 7th day after printing.

2.7. Cell viability and proliferation assays

The HFF cells (1.0×10^6 cells/mL) were added to 5%, 10%, 15%, and 20% concentrations of GelMA. Cell viability was measured by red or green fluorescent dye uptake with LIVE/DEAD® Viability/Cytotoxicity Kit. The samples were cultured in a humidified 5% carbon dioxide incubator at 37°C for 1, 3, and 7 days. The fluorescence images of the cell-laden structures were collected using confocal laser scanning microscopy (ZEISS LSM780, Oberkochen, Germany). Cell proliferation was determined using cell counting kit-8 assays (Medchemexpress, United States). The cells encapsulated in the GelMA were cultured in a humidified 5% carbon dioxide incubator at 37°C for 1, 2, 3, 4, 5, 6, and 7 days. The samples were incubated at 37°C for 2 h, and cell viability was quantified by measuring the ultraviolet absorbance of the solution at 450 nm using a microplate reader (RT-6100, Rayto, China).

2.8. F-actin fluorescent labeling

For the fluorescent staining of F-actin, the samples were washed twice in PBS and then fixed with 4% paraformaldehyde for 10 min at room temperature. After a 3× 10-min rinse with PBS, the samples were permeabilized with 5% Triton-X 100 for 3 min, washed thrice for 10 min in PBS, and stained with TRITC phalloidin for 30 min at 37°C in the dark. It was then washed thrice for 5 min in PBS. The samples were then counterstained with 100 nM 4′,6-diamidino-2-phenylindole (DAPI; Slarbio, China) for 15 min at room temperature in the dark and then washed twice for 5 min in PBS. The images of the samples were observed using confocal laser scanning microscopy (**Leica, Germany**) and analyzed using ImageJ software.

2.9. Western blot

Western blot was performed using a previously described method.[32] The HFF cells (1×10^6 cells/mL) encapsulated in the GelMA were cultured at 37°C and 5% carbon dioxide for 7 days. The samples were lysed in radioimmunoprecipitation assay buffer (Solarbio, China) with phenylmethanesulfonyl fluoride (Servicebio, China) on ice, followed by centrifugation for 5 min (12,000 rpm, 4°C). The protein was quantified using the bicinchoninic acid protein assay kit (HK Bio, China). The supernatants (10 μg protein) were subjected to SDS-PAGE (Servicebio, China) electrophoresis and transferred onto polyvinylidene difluoride membranes (Servicebio, China). The non-specific sites were blocked with 5% fat-free milk in tris-buffered saline with Tween-20 buffer (Servicebio, China) on a shaker at room temperature for 2 h. The membranes were then incubated with primary antibodies for collagen I (1:1000) and GAPDH (1:1000) (Servicebio, China) overnight at 4°C. Subsequently, the membranes were incubated with goat anti-Rabbit immunoglobulin

G, horseradish peroxidase secondary antibody (1:5000) (Abcam, United States) at room temperature for 2 h. Signal detection was performed using an enhanced chemiluminescence detection kit (Servicebio, China), and images were captured using the ChemiDoc XRS+ system (Bio-Rad, United States). Band intensities were quantified using ImageJ software.

2.10. Hematoxylin and eosin and Masson staining, immunohistology, and image analysis

The samples were fixed in 4% paraformaldehyde for 48 h and washed thrice for 5 min in PBS, followed by processing according to standard methods of paraffin wax embedding, dewaxing, and tissue sectioning. The samples were cut into 5-μm-thick sections using a microtome (RM2016, Leica, China) for hematoxylin and eosin (H&E) and Masson (BHBT, China) staining. The sections were immersed in xylene (I-20 min, II-20 min, and III-15 min) and sequentially immersed in ethanol solutions (100% twice, 85%, and 75%) for 5 min. Then, the sections were immersed in a hematoxylin solution for 5 min, washed with tap water for a minute, and dipped in 1% acid alcohol for 10 s. They were further immersed in a bluing solution for 5 min and then in an eosin Y solution for 2 min. After washing with tap water for a minute, the sections were sequentially immersed in a series of ethanol solutions (75%, 85%, 95%, and 100% twice) for 5 min in each solution for dehydration. After two immersions in xylene for 5 min each, the specimens were sealed with Neutral Balsam. Masson staining was performed following the instructions in the manual. Samples were visualized using an optical microscope (DMiLLED, Leica, China).

The sections (5 μm thick) were treated for epitope recovery and then incubated in 10% goat serum in PBS to block non-specific staining for immunohistological analysis. Skin sections were stained with rabbit antihuman (Abcam, United States) diluted in a 1:100 ratio in a 1× PBS solution containing 1% bovine serum albumin at 4 °C overnight, followed by washing and labeling with Alexa Fluor 488 goat anti-rabbit antibody (1:500; Abcam, United States) for an hour at room temperature. The sections were then counterstained with DAPI. The images of the samples were observed using confocal laser scanning microscopy. HUVECs suspension (1×10^6 cells/mL) was mixed with 3% GelMA hydrogels and cultured for 1, 7, and 14 days at 37 °C and 5% carbon dioxide, followed by staining with platelet endothelial cell adhesion molecule-1 (PECAM-1/CD31) immunofluorescence and F-actin fluorescence as described above.

2.11. Cell migration

To assess HUVEC migration in response to GelMA concentration gradients, a test model was constructed using 3–3% and 3–5% GelMA hydrogel pairings in the left–right regions of a 6-well plate. In each well, the left-hand region was filled with 3% (w/v) GelMA hydrogel containing HUVECs at a concentration of 1×10^6 cells/mL, while the right-hand region was filled with blank GelMA hydrogels at either 3% (w/v) or 5% (w/v), depending on the test condition. The culture medium was uniformly added over the hydrogels, and the plate was placed in an incubator. The migration behavior of HUVECs during the subsequent cultivation process was observed under the microscope.

2.12. Single concentration line fusion into the film plane printing

The GelMA with a concentration of 20% (w/v) was printed into samples with groove textures and smooth planar films by extrusion. After photocuring, HaCaT cell suspension was added to the surface and cultured in a 37°C 5% carbon dioxide incubator. Cell adhesion on the sample surface was recorded on the first and fifth days. The samples on the fifth day were used for cytoskeleton and nuclear staining.

2.13. Multi-concentration print layer fusion

The 20% (w/v) GelMA and 5% (w/v) GelMA bio-inks were prepared for layer printing, which was divided into full crosslinked printing (FCP) and partial crosslinked printing (PCP). For FCP, the bottom layer of 20% (w/v) GelMA ink was photocured for 100 s to achieve a higher degree of crosslinking. In contrast, for PCP, the bottom layer of 20% (w/v) GelMA ink was photocured for 10 s to limit crosslinking, while the upper layer of 5% (w/v) GelMA ink was photocrosslinked for 100 s. Frozen sections of the samples were made, and the cross sections were observed under a microscope. Meanwhile, the samples were soaked in the medium for 96 h, and after being taken out, a tensile test was performed using the method described previously.

2.14. Printing of vascularized skin substitutes

The 3% (w/v) GelMA bio-ink containing HUVECs (1×10^6 cells/mL) and blank 5% GelMA bio-ink were prepared. The extrusion method was used to construct circular dermal substitutes with microvascular network structures in the areas of the letters U, J, and ZJU. After 14 days, F-actin staining was performed as described previously. Bio-inks containing HFF cells (1×10^6 cells/mL) in 5% (w/v) GelMA and blank 20% (w/v) GelMA were prepared. The dermal layer and epidermal base were constructed using a layer-by-layer printing approach. After 14 days of culture in a Transwell, H&E and Masson staining were performed as described. Then, a 5% (w/v) GelMA layer containing HFF cells as the reticular layer, a 3% (w/v) GelMA layer containing HUVECs as the papillary layer, and a blank 20% (w/v) GelMA layer as the epidermal basal layer were sequentially built from the bottom up. HaCaT cells (1×10^7

cells/mL) were seeded onto the epidermal base to construct the skin substitute structure, and fluorescence staining was performed after 14 days of culture.

2.15. *BALB/c* nude mice and rabbit full-thickness excisional wound creation and transplantation

All animal procedures were performed according to the protocols approved by the Zhejiang University Health Sciences Animal Care and Use Committee. All experiments were performed following Animal Care and Use Committee guidelines and regulations. All mice were male *BALB/c* nude (n = 12; 4), aged 6 weeks and weighing between 16 and 20 g, were divided into three groups: untreated (control), blank GelMA (BG), and VS. A dimension of 2 × 1 cm^2 ($L \times W$) full-thickness skin was removed from the dorsal midline surface of mice, and a printed hydrogel was implanted into the wound. A Band-Aid was applied to cover the wounds. Then, the wounds were wrapped with sterile gauze and surgical tape to prevent bandage damage and photographed at 0, 1, 2, and 3 weeks, respectively. The mice were euthanized after 3 weeks for analysis. The New Zealand rabbits (n = 12; 3), aged 4 months and weighing between 2 and 3 kg, were divided into four groups: untreated (control), GelMA (blank), epidermis skin (E), and endothelial keratinocyte skin (EK). A dimension of 3 × 3 cm^2 ($L \times W$) full-thickness skin was removed from the dorsal of rabbits, and the wound was treated as described above. The wounds were photographed at 0, 1, 2, 3, and 4 weeks, respectively, and the rabbits were euthanized after 4 weeks for analyses.

2.16. Statistical analysis

All data analyses were performed using the Statistical Package for Social Sciences version 17.0. Statistical significance was analyzed using a one-way analysis of variance, with the Bonferroni method applied for multiple comparison corrections to adjust the p-values of individual tests. A p-value of ≤0.05 was considered statistically significant and marked with an asterisk (*). As the level of significance increased, the number of asterisks correspondingly increased. All data are presented as mean ± standard deviation.

3. Results and discussion

3.1. Replacing the sprinkler head: Positioning accuracy adjustment and print testing

The repeated positioning was randomly tested 10 times. After replacing the inner tube, the repeated positioning accuracy of the printhead in the XY plane was 104.93 μm. Since the printing structure is a single-layer membrane plane, the displacement deviation in the XY plane has a relatively small impact. This accuracy can meet the requirements of constructing a multi-layer skin structure by planar printing (Figure 2A). With excellent formability, the SA/gelatin composite hydrogel[33] was used for the extrusion printing of a five-pointed star model and a human ear model (Figure 2B). The printing system offers stable output and can construct complex, large-volume hydrogel tissues, meeting the requirements for skin substitute printing. The height of the printed multi-layer model can reach over 4 mm (Figure 2C), meeting the thickness requirement of 1–4 mm for human skin.[34] The multi-layer structure of the model is visible, which meets the construction requirements of the multi-layer skin substitutes in this study.

3.2. Characterization of gelatin methacryloyl

The proton nuclear magnetic resonance spectroscopy spectra (Figure 3A) showed the degree of modification of methacryloyl groups to gelatin molecules. The appearance of peaks at δ = 5.4 and 5.7 ppm (the protons of the methacrylate vinyl group of methacryloyl) and the disappearance of peak at δ = 3.0 ppm (the protons of the methylene of lysine signal) indicated that methacryloyl was successfully grafted on the gelatin. Using the peak area normalization method, the degree of functionalization of GelMA samples was improved from 30% to 90%.

The results of tensile and compression tests are shown in Figure 3B and C. The data interval in the strain range of 2–10% was selected to calculate the elastic modulus. It was observed that the mechanical properties of the tensile modulus and the compression modulus of GelMA hydrogels with different concentrations become stronger as the concentration increases. This characteristic provides a theoretical basis for studying the functional performance of skin cells in GelMA with varying concentrations.

Hydrogel swelling is a phenomenon where the hydrogel absorbs water and increases in volume. The swelling is caused by the balance between osmotic pressure and elastic force. The osmotic pressure results from the difference in solute concentration inside and outside the hydrogel. This difference drives water molecules to penetrate from the low-concentration region to the high-concentration region, thus causing the hydrogel to expand. The elastic force comes from the cross-linking points between polymer chains and entropy elasticity, which work together to resist excessive expansion. Figure 3D shows that the swelling ratio of GelMA hydrogels is negatively correlated with the concentration, and there are significant differences among groups. This can directly reflect the pore structure of the hydrogel. Generally, the pore structure is also larger for hydrogel components with a larger swelling ratio.

Scanning electron microscopy (Figure 3E) reveals significant differences in pore structure sizes among groups. Wang *et al.*[35] demonstrated that larger pores facilitate more

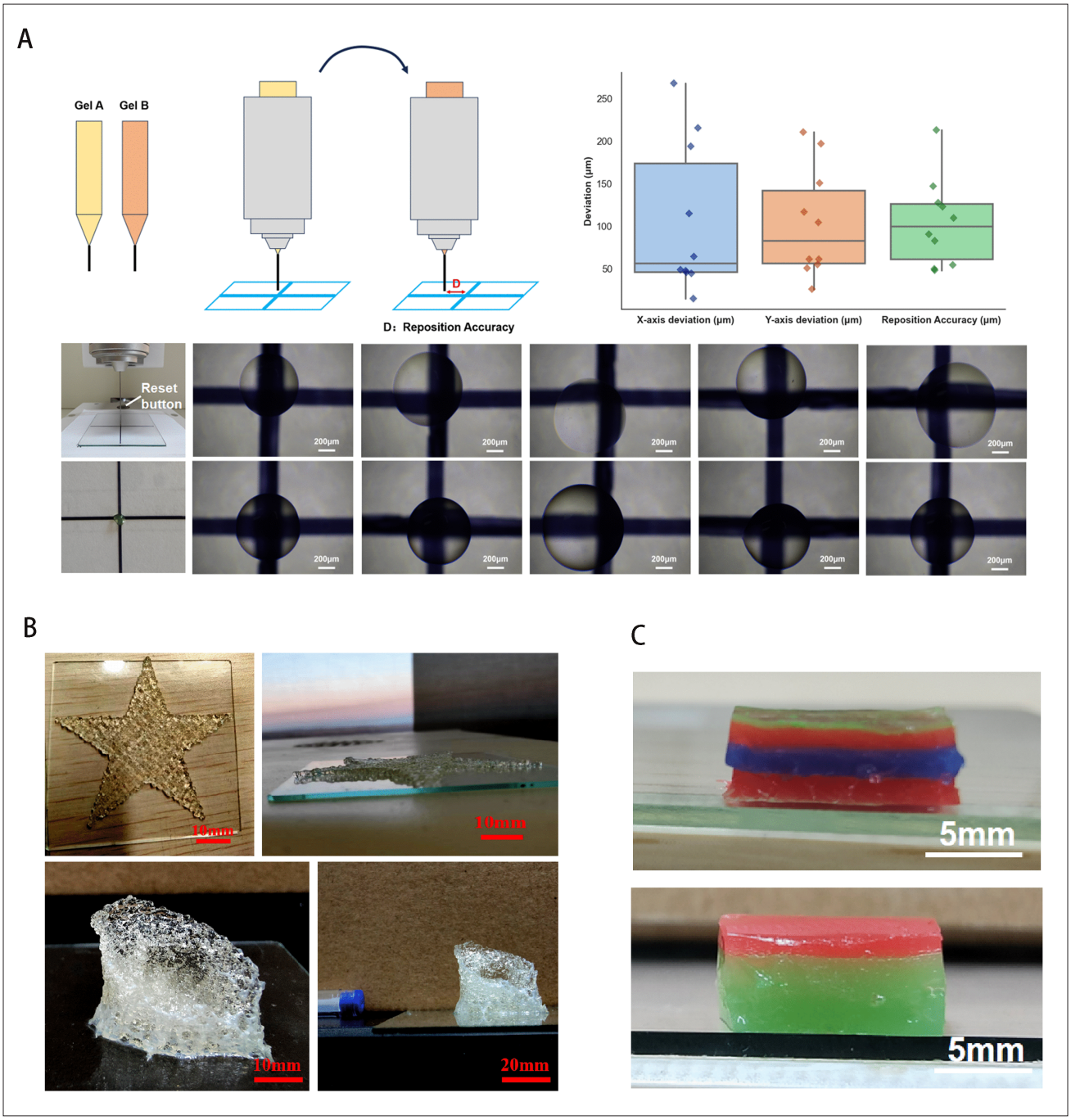

Figure 2. Printing device testing. (A) Principle of the printhead repeatability positioning test, repeatability positioning test values, and representative microscopy images of the repeatability positioning test. Scale bar: 200 μm. (B) Sodium alginate/gelatin printed five-pointed star and human ear models. Scale bar: 10 and 20 mm. (C) Multi-layered structure printing tests of 10% (w/v) gelatin methacryloyl with different dyes. Scale bar: 5 mm.

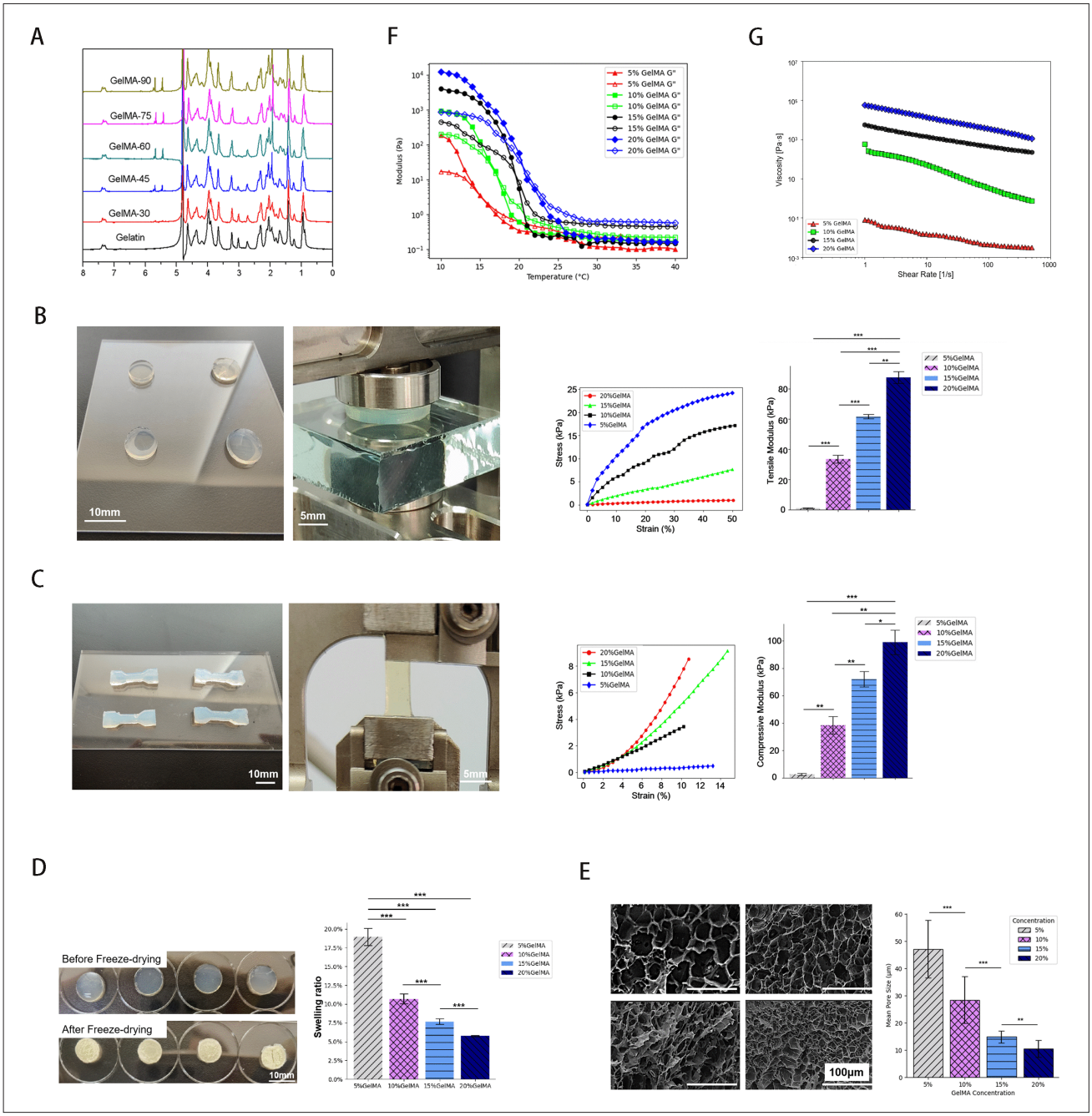

Figure 3. Characterization of gelatin methacryloyl (GelMA). (A) Quantification of the degree of functionalization of GelMA using proton nuclear magnetic resonance spectroscopy. (B) Compression testing of samples, experimental procedures, and quantification of compression modulus. Scale bars: 5 and 10 mm. (C) Tensile testing of samples, experimental procedures, and quantification of tensile modulus. Scale bars: 5 and 10 mm. (D) Samples of GelMA before and after freeze-drying, and quantification of swelling ratio. Scale bar: 10 mm. (E) Scanning electron microscopy images of GelMA: representative electron micrographs and quantification of GelMA porosity. Scale bar: 100 μm, magnification 500×. (F) Determination of gelation point in GelMA hydrogels. (G) Rheological characterization of GelMA. Data were analyzed via a one-way analysis of variance and are shown as mean ± standard deviation (*$p < 0.05$, **$p < 0.01$, ***$p < 0.001$, $n = 3$). For a better overview, only the significant differences are indicated.

efficient transport of nutrients and oxygen while providing sufficient space for cell attachment and extension, enabling them to perform their biological functions. Human fibroblasts and vascular endothelial cells are relatively large, necessitating the selection of hydrogels with larger pores, i.e., lower-concentration GelMA hydrogels, as carriers for printing.

The rheological properties of hydrogels directly influence the material flow and molding quality during the printing process. Rheology refers to the property of hydrogels to deform and recover under external force. Figure 3F indicates that for GelMA of all concentrations, both G' and G'' decrease as the temperature rises, but the decrease rate of G' is greater. The intersection point of G' and G" represents the gel point. When the temperature is lower than the gel-point temperature, $G' > G''$ for the hydrogel shows a solid state; conversely, above the gel point, where $G'' > G'$, it shows a liquid state. Figure 3G shows the "shear-thinning" phenomenon of GelMA hydrogels, where the viscosity decreases as the shear rate increases. This may be because when subjected to a large shear force, the entanglement points of the polymer chains inside the hydrogel are opened, and the structure undergoes directional stretching, resulting in a decrease in viscosity. Kim *et al.*[36] and Won-woo *et al.*[37] have demonstrated the shear-thinning behavior of porous hydrogels.

3.3. Printability and biocompatibility

The printing test results are shown in Figure 4A. All GelMA hydrogels of different concentrations have a printable interval and can form a stable and regular two-layer hydrogel grid structure. When the concentration of GelMA hydrogel increases, its suitable printing pressure and temperature will also increase. For a single concentration of GelMA, if the printing pressure or temperature is too low, over-gelling and irregular extrusion will occur. Conversely, under-gelling and excessive softening extrusion will occur if the printing pressure or temperature is too high.

Cell viability staining (Figure 4B) shows that HFF cells' survival rates for both mesh and membrane structures on Day 0 and Day 7 are greater than 90%, and the cell viability increased with prolonged culture time. This indicates that GelMA is a hydrogel bio-ink with excellent biocompatibility, allowing cells to maintain good vitality. Song *et al.*[38] demonstrated that bio-inks made from GelMA exhibit cell morphology on the first day of cell seeding on the GelMA bio-ink, with cell confluence exceeding 90% by the seventh day.

3.4. Skin cells adapted to composite ink

The HFF cell line is derived from human neonatal foreskin tissue. It has the normal functions of human fibroblasts, such as secreting extracellular matrix and growth factors, and is often used to study the role of fibroblasts in tissue repair and regeneration. HFF cells have a high survival rate at 5%, 10%, 15%, and 20% (w/v) GelMA (Figure 5A and C). On the first day, HFF cells in the 5% (w/v) GelMA group had slightly extended. By the seventh day, almost all cells in the 5% (w/v) GelMA group had extended and multiplied exponentially. In the 10% (w/v) GelMA group, only some cell extension and a small amount of proliferation were observed, while cells in other groups remained spherical. When HFF cells in the 5% (w/v) GelMA group were cultured until the tenth day, the cells extended into long, spindle-shaped structures, and the extension length exceeded 200 μm (Figure 5B). Type I collagen is a fibrous collagen that maintains tissue elasticity in the human dermis and is mainly secreted by fibroblasts. Fibrinogen, as a natural biomaterial with excellent biocompatibility, is a key material for manufacturing skin substitutes in traditional tissue engineering.[39] According to the numerical analysis of the gray value, the content of type I collagen in the 5% (w/v) GelMA group is significantly higher than that in the high-concentration groups but slightly lower than that in the fibrinogen group (Figure 5D). Therefore, among GelMA groups with different concentrations, 5% (w/v) GelMA is more suitable for the functional performance of human skin fibroblasts.

The human skin epidermis mainly comprises keratinocytes, melanocytes, and Langerhans cells. Keratinocytes are derived from the ectoderm and account for over 90% of human epidermal cells. Scholars have conducted extensive research on the culture methods of keratinocytes. Research shows that keratinocytes must be cultured under air–liquid interface conditions to differentiate into a multi-layer epidermal structure *in vitro*.[40-42] Keratinocytes can attach and proliferate on the surfaces of 5%, 10%, 15%, and 20% (w/v) GelMA solidified through manual dropping (Figure 5E). On Day 2, HaCaT cells in the 20% (w/v) group grew in a sheet-like manner. By Day 5, HaCaT cells in the 20% (w/v) group formed a film and covered the hydrogel surface, which was significantly better than the other three groups. Moreover, higher concentration results in better attachment and proliferation of HaCaT cells throughout the growth and reproduction cycle. By Day 10, there was an obvious basal-epidermal layer interface in the 20% (w/v) GelMA group and the collagen group, with clear epidermal structures, and the thicknesses were 53.63 ± 11.27 and 52.26 ± 26.33 μm, respectively. By Day 28, a relatively thick epidermal layer structure could be seen in both groups of samples, with thicknesses of 130.61 ± 8.84 and 119.29 ± 18.87 μm, respectively, both approaching the 200 μm thickness of the human epidermis. However, the printed GelMA group

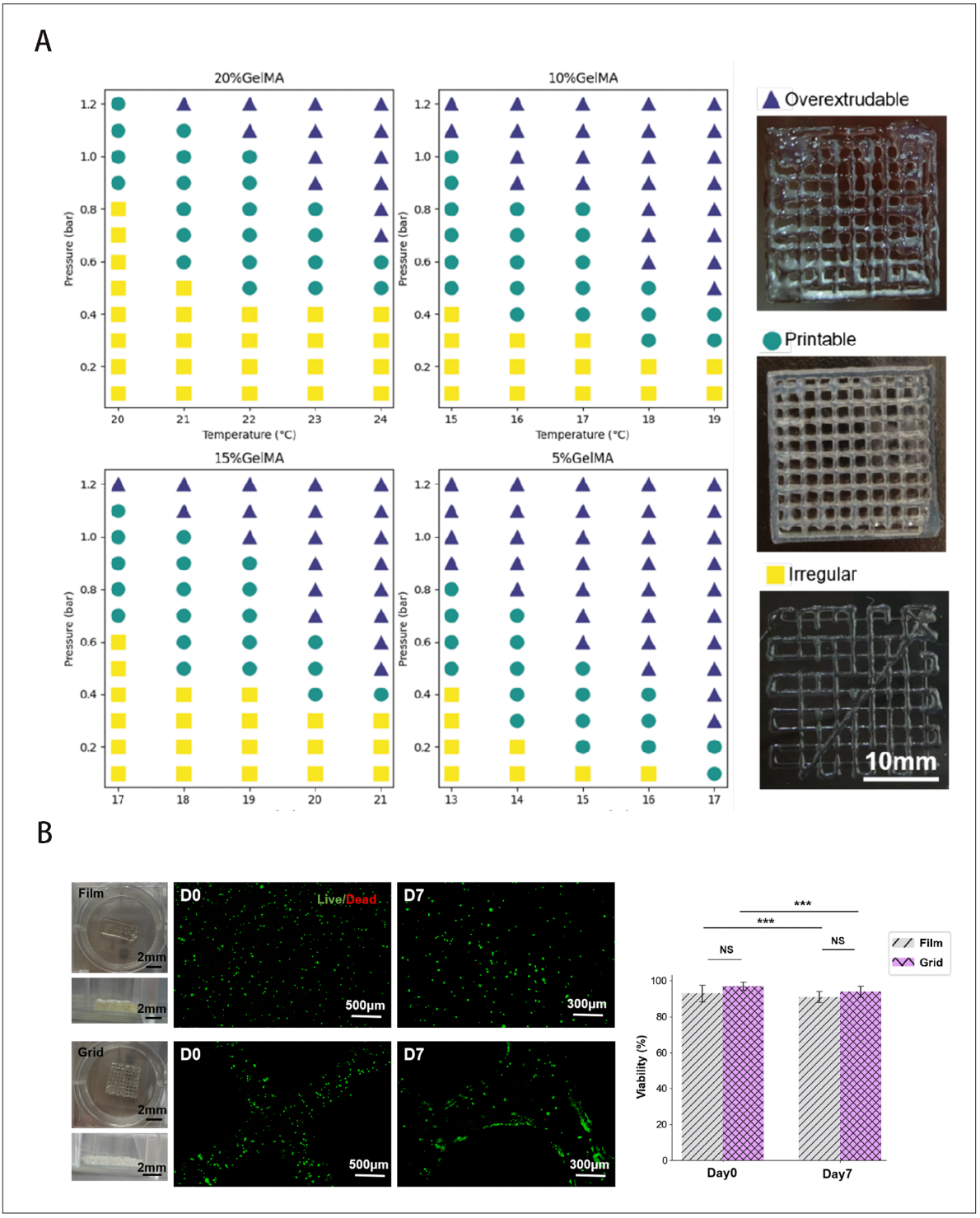

Figure 4. Printability and biocompatibility of gelatin methacryloyl (GelMA). (A) Printing tests of GelMA at different concentrations under varying temperatures and pressures. Overextrudable: GelMA is overly softened during extrusion, and the extruded material cannot maintain its original linear structure after exiting the nozzle, resulting in softening, collapse, and formation of lines with uneven widths. Printable: GelMA is smoothly extruded, forming continuous and stable linear structures. Irregular: GelMA is irregularly extruded, with intermittent or discontinuous extrusion from the nozzle, leading to broken lines and discontinuous structures. Scale bar: 10 mm. (B) Human foreskin fibroblast cells-laden printing examples of 10% (w/v) GelMA in membrane/grid forms, with live/dead staining microscopy images at Day 0 and Day 7, and quantification of cell viability using ImageJ. Data were analyzed via a one-way analysis of variance and are shown as mean ± standard deviation (*$p < 0.05$, **$p < 0.01$, ***$p < 0.001$, $n = 3$). Scale bars: 2 mm, 300 μm, and 500 μm; magnification: 100× and 40×.

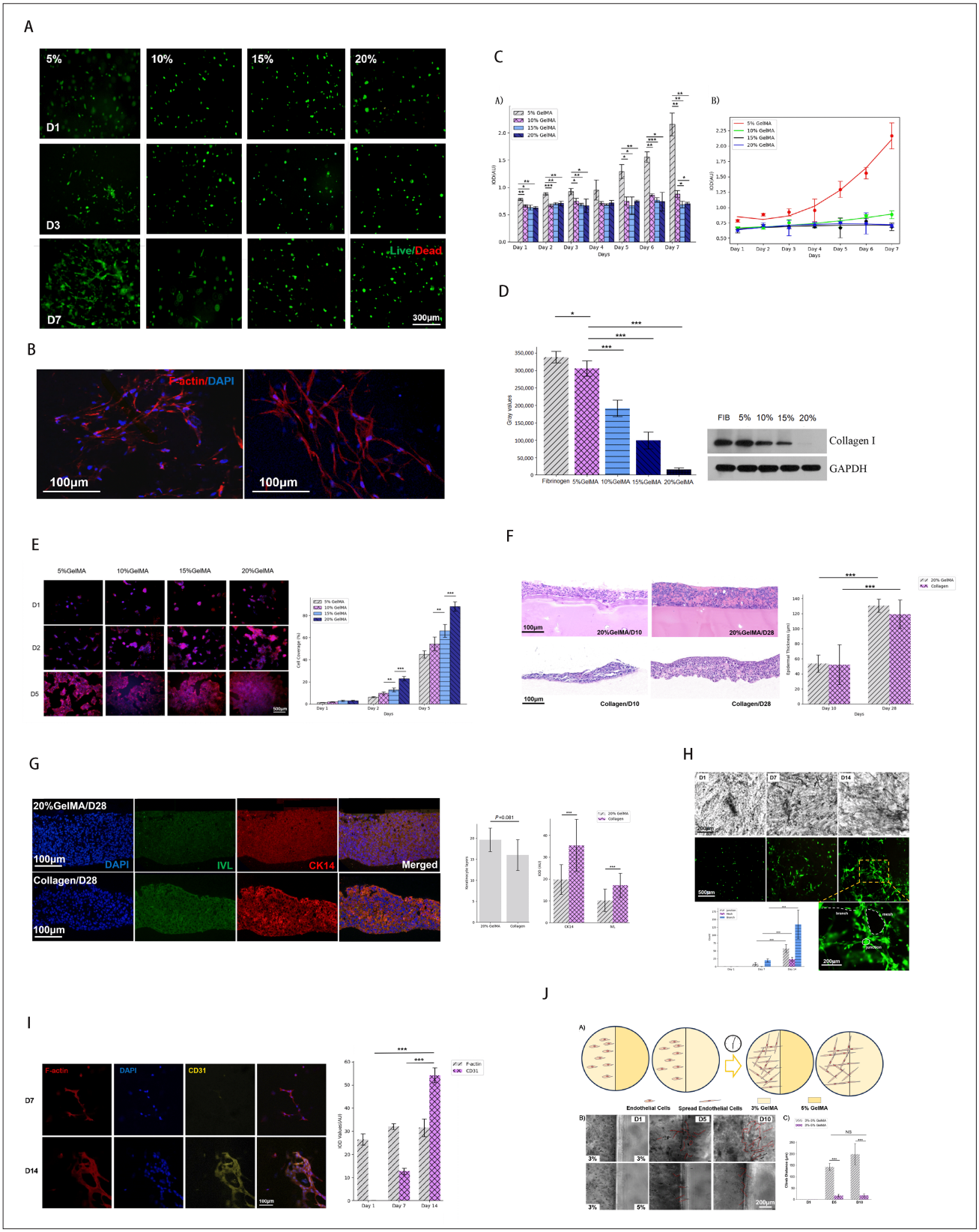
A
5%
10%
15%
20%
D1
D3
D7
Live/Dead
300μm
B
F-actin/DAPI
100μm
100μm
C
A)
5% GelMA
10% GelMA
15% GelMA
20% GelMA
IOD/AU
Day 1 Day 2 Day 3 Day 4 Day 5 Day 6 Day 7
Days
B)
5% GelMA
10% GelMA
15% GelMA
20% GelMA
IOD/AU
Day 1 Day 2 Day 3 Day 4 Day 5 Day 6 Day 7
Days
D
Gray values
Fibrinogen 5%GelMA 10%GelMA 15%GelMA 20%GelMA
FIB 5% 10% 15% 20%
Collagen I
GAPDH
E
5%GelMA
10%GelMA
15%GelMA
20%GelMA
D1
D2
D5
500μm
Cell Coverage (%)
Day 1 Day 2 Day 5
Days
F
100μm
20%GelMA/D10
20%GelMA/D28
100μm
Collagen/D10
Collagen/D28
Epidermal Thickness (μm)
Day 10 Day 28
Days
20% GelMA
Collagen
G
20%GelMA/D28
100μm
DAPI
IVL
CK14
Merged
Collagen/D28
100μm
P=0.081
Keratinocyte layers
20% GelMA Collagen
IOD /AU
CK14 IVL
H
D1
D7
D14
200μm
500μm
branch
mesh
lumen
200μm
I
D7
D14
F-actin
DAPI
CD31
100μm
IOD Values(AU)
Day 1 Day 7 Day 14
F-actin
CD31
J
A)
Endothelial Cells
Spread Endothelial Cells
3% GelMA
6% GelMA
B)
D1
D5
D10
3%
3%
3%
5%
200μm
C)
NS
D1 D5 D10

Figure 5. Skin cell-compatible composite ink. (A) Live/dead staining to assess the viability and stretching of human foreskin fibroblast (HFF) cells in 5%, 10%, 15%, and 20% (w/v) gelatin methacryloyl (GelMA). Scale bar: 300 μm; magnification: 50×. (B) F-actin/4′,6-diamidino-2-phenylindole (DAPI) staining of HFF cells cultured in 5% (w/v) GelMA for 10 days. Scale bar: 100 μm. (C) Cell counting kit-8 (CCK-8) assay to measure the proliferation of HFF cells in 5%, 10%, 15%, and 20% (w/v) GelMA from Day 1 to Day 7. (D) Western blot analysis of collagen I protein expression in HFF cells cultured in 5%, 10%, 15%, and 20% (w/v) GelMA, quantifying collagen I expression using ImageJ. (E) Proliferation of human immortalized epidermal cells (HaCaT) cells on the surface of 5%, 10%, 15%, and 20% (w/v) GelMA, with quantification of HaCaT cells surface coverage using ImageJ. Scale bar: 500 μm. (F) Hematoxylin and eosin staining of HaCaT cells cultured on 20% (w/v) GelMA and collagen surfaces for 10 and 28 days, with quantification of epidermal thickness using ImageJ. Scale bar: 100 μm; magnification: 50×. (G) Immunofluorescence staining of Involucrin (IVL) and Cytokeratin 14 (CK14) in HaCaT cells cultured on 20% (w/v) GelMA and collagen surfaces for 10 and 28 days, with quantification of keratinocyte layer number and IVL/CK14 expression using ImageJ. Scale bar: 100 μm. (H) Fluorescence microscopy images of human umbilical vein endothelial cells (HUVECs) spreading in 3% (w/v) GelMA at D1, D7, and D14, with quantification of junction, mesh, and branch formation using ImageJ. Scale bars: 200, 500 μm; magnification: 50×. (I) Immunofluorescence staining of platelet endothelial cell adhesion molecule-1 (PECAM-1/CD31) and F-actin in HUVECs cultured in 3% (w/v) GelMA at Day 7 and Day 14, quantifying CD31 and F-actin expression using ImageJ. Scale bar: 100 μm. (J) Schematic diagram of the HUVECs migration experiment from 3% (w/v) GelMA to 3% (w/v) GelMA or 5% (w/v) GelMA, with microscopy images of cell migration at D7 and D14, and quantification of migration distance using ImageJ. Scale bar: 200 μm; magnification: 50×. The red dashed lines mark areas where partial cell extension and interconnected microvascular structures are observed. Data were analyzed via a one-way analysis of variance and are shown as mean ± standard deviation ($^{*}p < 0.05$, $^{**}p < 0.01$, $^{***}p < 0.001$, $n = 3$). For a better overview, only the significant differences are indicated. Abbreviations: ALI, air–liquid interface; FIB, fibrinogen; GAPDH, glyceraldehyde-3-phosphate dehydrogenase; IOD, integrated optical density

displayed a more uniform and flat epidermal structure (Figure 5F). Involucrin (IVL) is a highly reactive soluble transamidase substrate protein present in keratinocytes of the epidermis and other stratified squamous epithelia, synthesized in the spinous layer. It is highly expressed in the granular layer and serves as a marker of the terminal differentiation of keratinocytes. Cytokeratin 14 (CK14) is a member of the intermediate fiber albumen type I keratin family that pairs with type II keratin CK5 to form the basic keratin of stratified squamous epithelial keratinocytes, including the epidermis and non-keratinized stratified squamous epithelial mucosa. It is highly expressed in the undifferentiated basal cell layer, containing stem cells, and down-regulated in differentiated basal cell layers. The GelMA and collagen groups had a cell structure of more than 10 layers, with no obvious difference between them, similar to the structure of the human skin epidermis. CK14 and IVL were significantly expressed in the GelMA and fibrinogen groups (Figure 5G). The observed pattern of CK14 and IVL co-expression in the same region may be attributed to the unique microenvironment of *in vitro* culture, where the differentiation process of keratinocytes might not fully replicate the *in vivo* scenario, leading to overlapping expression of markers that are typically spatially separated. The 20% (w/v) GelMA is more conducive to the growth and proliferation of HaCaT cells on its surface, and the keratinocytes on its surface have a high degree of functional expression. Therefore, 20% (w/v) GelMA loaded with HaCaT cells was selected as the bio-ink for constructing the epidermal base layer.

The human vascular system is a complex and precise network that spreads throughout the body and is responsible for transporting oxygen and nutrients to all body parts while removing waste and carbon dioxide through blood circulation. In the subcutaneous tissue, there are arterioles and venules. The arterioles and venules, formed by their branching, pass through the dermis and form a rich microvascular network in the upper layer of the dermis (papillary layer), which supplies oxygen and nutrients to the epidermis.[43,44] The construction of the microvascular network in the upper layer of the dermis is of great significance for the construction of the skin epidermal barrier function. As shown in Figure S1, Supporting Information, HUVECs were cultured in 3% (w/v), 5% (w/v), and 7% (w/v) GelMA hydrogels, respectively, and observed under a microscope every 3 days for imaging. In the 3% (w/v) GelMA hydrogel group, HUVECs began to extend and elongate by Day 3, and extensive microvascular formation was observed by Day 9. In the 5% (w/v) GelMA hydrogel group, slight cell elongation was noted by Day 9, while no significant changes were observed in the 7% (w/v) GelMA hydrogel group. In conclusion, the 3% (w/v) GelMA hydrogel is more suitable for HUVEC culture. When the 3% (w/v) GelMA bio-ink containing HUVEC-green fluorescent protein (1×10^6 /mL) was cultured for 7 days after solidification, the vascular endothelial cells began to spread and intersect to form some connection points, showing a tube-forming phenomenon. On the 14th day, the tube-forming effect of vascular endothelial cells was apparent, producing many branches, connection points, and grid structures (Figure 5H). PECAM-1/CD31 is a transmembrane glycoprotein belonging to the immunoglobulin superfamily. It is a major marker of vascular endothelial cells. It is often used to identify the structure of vascular endothelial cells, and its expression level can reflect the functionality of vascular endothelial cells.[45] During the incubation of 3% (w/v) GelMA bio-ink containing HUVEC-green fluorescent protein (1×10^6 /mL) from 7 to 14 days, the expression of CD31 in vascular endothelial cells increased

(Figure 5I), indicating that when vascular endothelial cells form tubes, the intercellular signal transduction and other interaction mechanisms may occur more intensively, and the cell functional activities are more frequent.

In the 3% (w/v) GelMA samples, HUVECs exhibited spreading by Day 5. Cell migration into the blank hydrogel was observed in the 3–3% (w/v) test samples, with a migration distance of 197.12 ± 47.51 μm by Day 10, nearly equivalent to the length of a single HUVEC. In contrast, no migration was observed in the 3–5% (w/v) test samples, with no significant change in migration distance between Days 5 and 10 (Figure 5J). This may be because the small pore structures within the higher-concentration hydrogel restrict the inward growth of HUVECs. This property supports the controlled construction of microvascular network distribution regions, enabling the formation of a papillary layer with a microvascular network and a reticular layer without one. A VS substitute with distinct layered characteristics can be constructed based on this.

3.5. Single-concentration line fusion for planar film printing and multi-concentration layer fusion

Numerous studies have confirmed that the morphology and mechanical properties of hydrogel substrates have

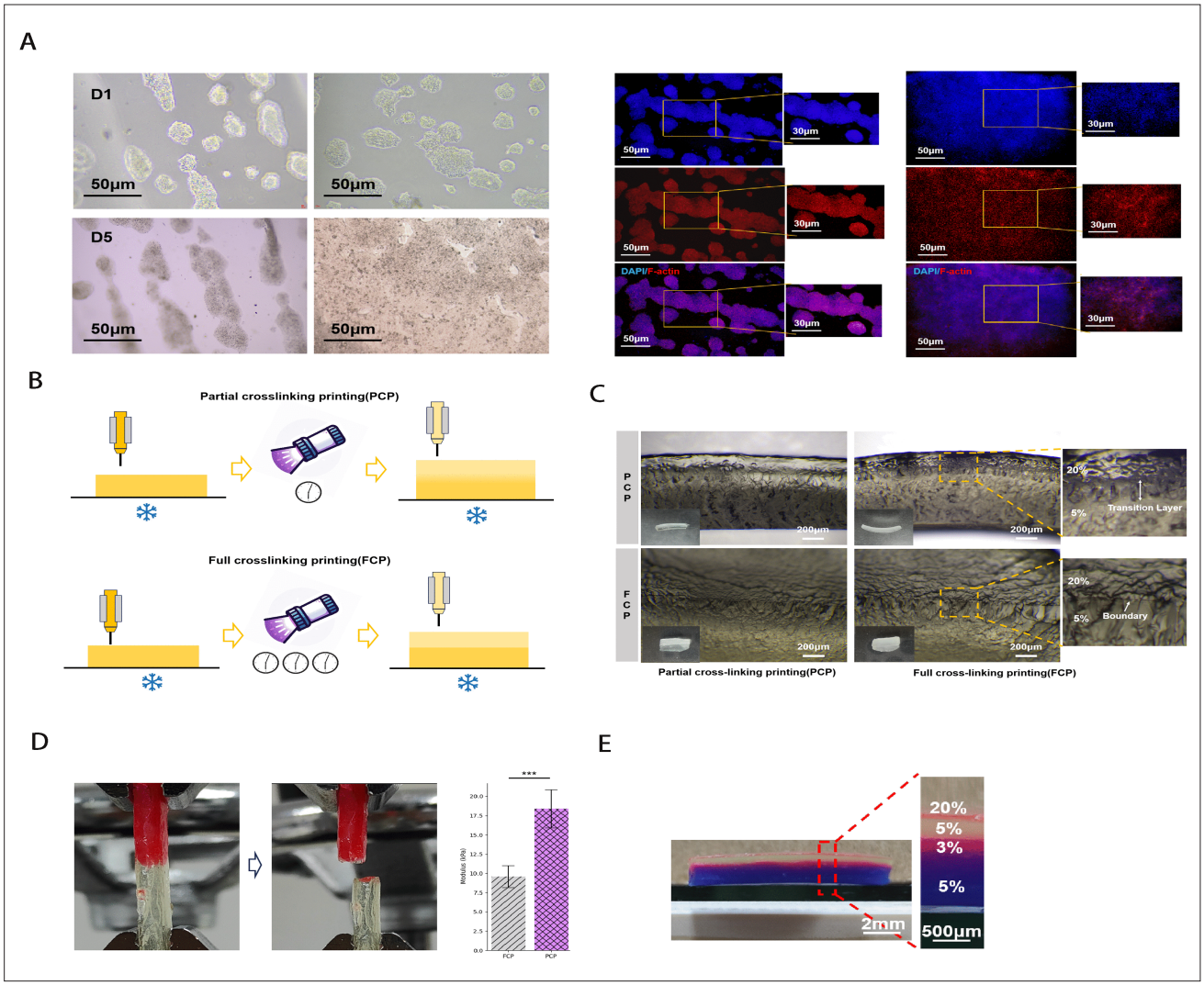

Figure 6. Single-concentration line fusion and multi-concentration layer fusion of gelatin methacryloyl. (A) Exemplary microscope images of human immortalized epidermal cells on grooved and flat substrates at Day 1 and Day 5, with F-actin and 4′,6-diamidino-2-phenylindole staining (DAPI) at Day 5. Scale bars: 50 and 30 μm; magnification: 40× and 100×. (B) Schematic diagram of the partial concentration printing (PCP) and full concentration printing (FCP) layer fusion printing processes. (C) Exemplary microscope images of the interface in PCP and FCP layer fusion printing. Scale bar: 200 μm; magnification: 40×. (D) Tensile testing of the layered fusion printed structures, showing significant differences in tensile modulus between PCP and FCP; statistical significance at ***$p < 0.005$. (E) Multi-layered skin structure model printed using the FCP layer fusion method. Scale bars: 2 mm and 500 μm.

a significant impact on the growth characteristics of cells, such as cell-oriented growth and the degree of differentiation and maturation.[46-48] HaCaT cell suspension was dropped onto the surface of 20% (w/v) GelMA samples with groove textures and smooth planar film, respectively. On Day 1, HaCaT cells on the grooved samples exhibited a clear tendency to grow along the grooves, while cells on the smooth planar membranes appeared scattered and clustered. By Day 5, HaCaT cells on the grooved samples continued to grow along the grooves without forming a continuous layer. In contrast, cells on the smooth planar membranes had largely converged into a continuous layer (Figure 6A).

The multi-concentration layer fusion process is shown in Figure 6B. The cross-sectional images show that the bilayer structure printed using the PCP method exhibited a transitional layer, whereas the structure printed using the FCP method showed a distinct boundary between layers (Figure 6C). To quantify the interlayer bonding strength, the samples were cultured *in vitro* for 96 h to simulate the skin substitute. Tensile testing results (Figure 6D) revealed that the fracture strength at the bonding interface of FCP was 9.6 ± 1.4 kPa, while that of PCP was 18.4 ± 2.5 kPa. The PCP method effectively enhanced the bonding strength between different layers, increasing it by 91.67% compared with the FCP method. The reason may be that the upper-layer ink in the PCP printing method can form an intertwined structure with the lower-layer ink, thus improving the inter-layer bonding strength. Based on the PCP process, a four-layer skin model was printed by mixing pigments into inks of different concentrations (Figure 6E). The thickness of each layer can be controlled to vary, with the thick layer exceeding 1 mm and the thin layer less than

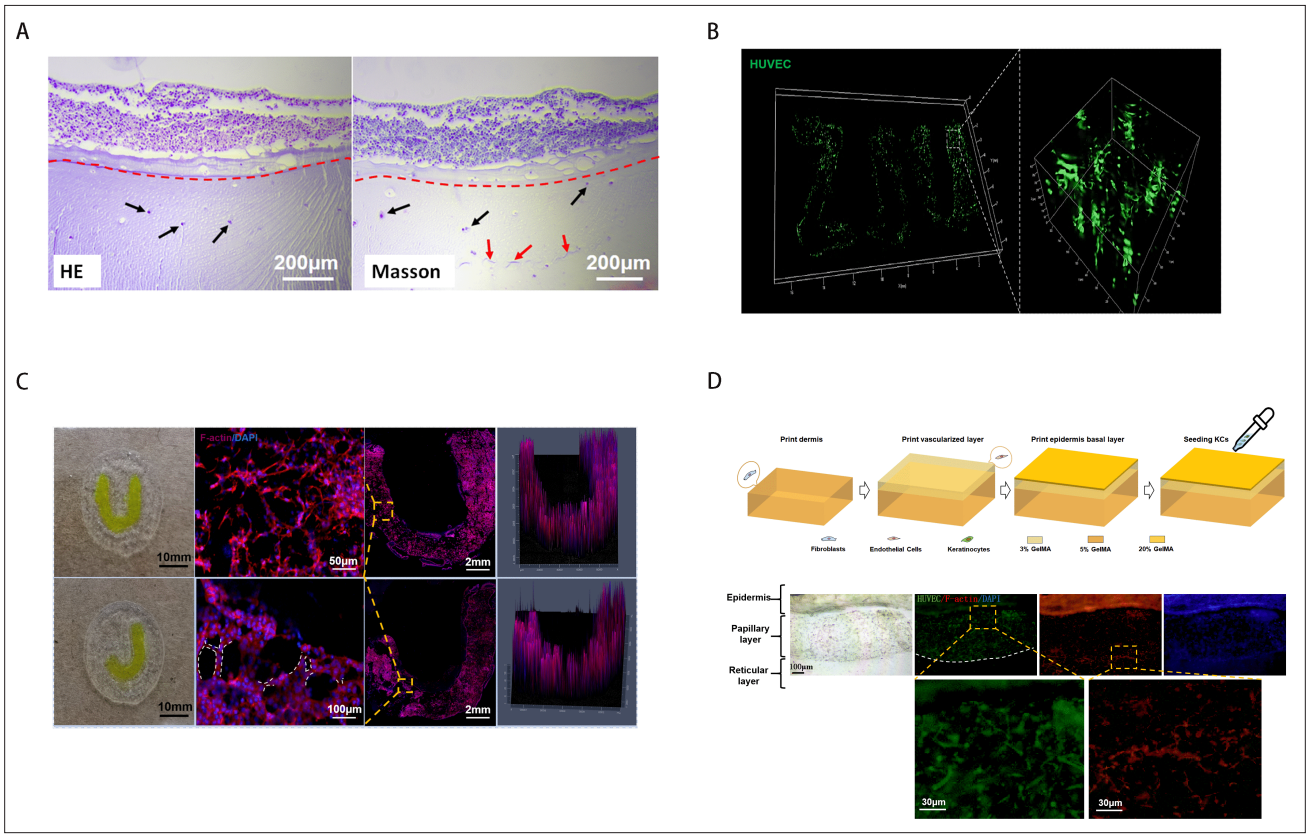

Figure 7. Printed vascularized skin substitutes. (A) Hematoxylin and eosin (HE) and Masson staining of the bilayered skin. The red dashed line indicates the dermo-epidermal junction, black arrows point to fibroblast nuclei in the dermis, and red arrows indicate collagen fibers. Scale bar: 200 μm, magnification: 40×. (B) Laser confocal microscopy images of vascularization in a defined ZJU region within human umbilical vein endothelial cells (HUVECs)-laden gelatin methacryloyl (GelMA). (C) Exemplary confocal microscopy images of self-assembled microvascular networks forming "U" and "J" shapes. The "U" and "J" shapes were printed using 3% (w/v) GelMA containing HUVECs, while the surrounding area was printed using blank 5% GelMA. Scale bars: 10 mm, 2 mm, 50 μm, and 100 μm; magnification: 100×. (D) Schematic diagram of the construction of vascularized dermal skin. Vascularized dermal models were constructed and subjected to immunofluorescence staining: green fluorescent protein for HUVECs, F-actin for HaCaT cells and human foreskin fibroblast (HFF) cells, and DAPI for nuclei of HUVECs, HaCaT cells, and HFF cells. The white dashed line indicates the boundary between the papillary and reticular layers. Scale bar: 30 and 100 μm.

60 μm. The layers exhibited clear morphology and stable printing structure.

3.6. Printing of vascularized dermal skin substitutes

The vascularized dermal skin substitute comprises the epidermis, papillary, and reticular layers. Initially, a bilayer skin substitute of the dermis and epidermis was constructed (Figure 7A), followed by a dermal substitute with a controllable microvascular network distribution (Figure 7B and C). These were then integrated to create a vascularized dermal skin substitute with a dermal-epidermal interface and a microvascular network in the papillary layer (Figure 7D). After 14 days of culture in a Transwell, the bilayer skin substitute exhibited distinct dermal and epidermal layers. The red dashed line in the figure shows the interface between the 20% and 5% (w/v) GelMA layers of the dermal and epidermal layers, respectively. The black arrow in the figure points to the nucleus of fibroblasts in the dermis, and the red arrow points to the collagen fibers stained by Masson, indicating that fibroblasts in this structure have exerted biological functions and synthesized and secreted collagen (Figure 7A). Trujillo *et al.*[49] demonstrated that encapsulating microcarriers seeded with HUVECs into a vascular endothelial growth factor (VEGF)-containing hydrogel resulted in extensive vascular sprouting similar to that observed in Matrigel. In contrast, our study utilized pure GelMA hydrogel without the addition of VEGF and successfully constructed a disc-

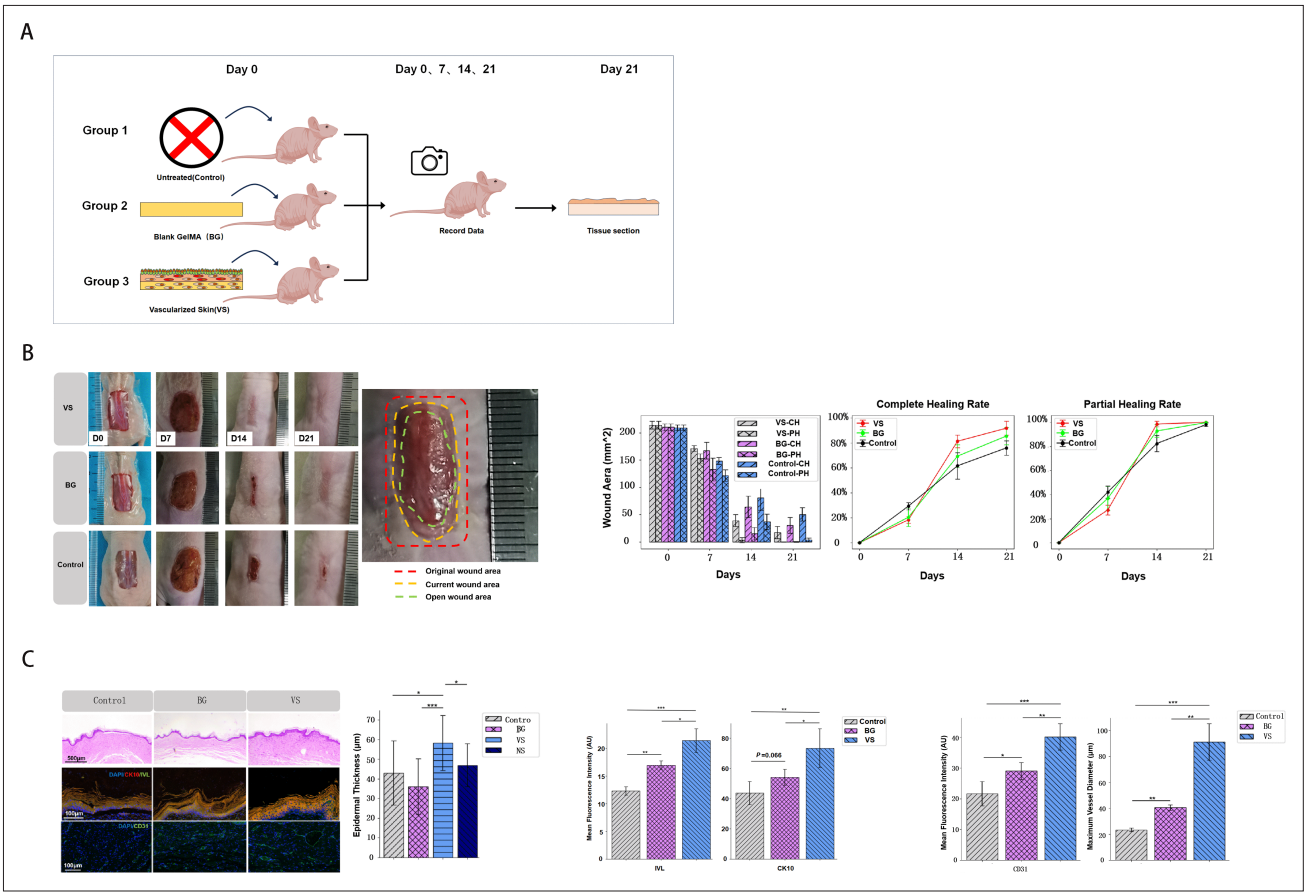

Figure 8. Repair of dorsal skin defects in *BALB/c* nude mice. (A) Flowchart of the dorsal skin defect repair experiment in *BALB/c* nude mice. (B) Photographs of dorsal skin defect healing in *BALB/c* nude mice at Day 0, Day 7, Day 14, and Day 21. By Day 21, the partial healing rates in all three groups were close to 100%, with no significant differences. However, there were significant differences in the complete healing rates of the epidermis among the three groups. The vascularized skin (VS) group showed a significantly higher complete healing rate (91.78 ± 5.42%) compared to the blank gelatin methacryloyl (BG) group (85.51 ± 6.96%) and the control group (75.99 ± 5.81%). (C) Hematoxylin and eosin (HE) and immunohistochemical staining of the healed dorsal skin defects in *BALB/c* nude mice. HE indicated significant differences in epidermal thickness between the VS and other groups. The expression of involucrin (IVL) and cytokeratin 10 (CK10) proteins in the newly formed epidermis of the dorsal skin showed significant differences between the VS group and the control and BG groups. Additionally, platelet endothelial cell adhesion molecule-1 (PECAM-1/CD31) expression and the maximum vascular diameter in the newly formed skin significantly differed between the VS group and the control and BG groups. Data were analyzed via a one-way analysis of variance and are shown as mean ± standard deviation (*$p < 0.05$, **$p < 0.01$, and ***$p < 0.001$, $n = 3$). For a better overview, only the significant differences are indicated. Scale bars: 100 μm and 500 μm; magnification: 100× and 40×. Abbreviations: CH, complete healing; PH, partial healing.

shaped dermal substitute featuring microvascular network structures in the shapes of "U," "J," and "ZJU" letter patterns (Figure 7B and C). After 14 days of culture, the tube-forming phenomenon was evident within the letter structures, with distinct interconnected branches and grid structures. The microvascular network was well-formed and confined to the areas of lower-concentration ink, without migrating to regions of higher-concentration ink. The structures marked by the white dotted line represent the tube-forming branches, indicating that the lumen diameter of the self-assembled microvessels is between 5 and 20 μm. From the fluorescence staining of the structure of the constructed skin substitute (Figure 7D), it can be seen that each layer is stratified. The cells in the reticular, papillary, and epidermal layers are orderly distributed according to the layer structure. Among them, the HFF cells in the reticular layer and the HUVECs in the papillary layer are spread and elongated.

3.7. Validation of printed vascularized skin substitutes in mice

BALB/c nude mice are an immunodeficient experimental animal model that shows no rejection reaction to many foreign tissues and cells.[50] Moreover, *BALB/c* nude mice have completely hairless skin, making them a suitable experimental animal for skin-healing evaluation.[51] The skin injury repair experiment process in *BALB/c* nude mice is illustrated in Figure 8A. The healing progress of the dorsal wounds was regularly photographed and recorded, and ImageJ was used to quantitatively measure the wound areas of complete and partial healing. At 21 days, the partial healing rates for all three groups were close to 100%, with the VS group at 100 ± 0%, the BG group at 99.75 ± 0.51%, and the control group at 98.08 ± 1.46%. However, there were significant differences in the degree of complete epidermal healing. The VS group had a significantly higher complete healing rate (91.78 ± 5.42%) compared to the BG group (85.51 ± 6.96%) and the control group (75.99 ± 5.81%) (Figure 8B). This phenomenon may be because the VS substitute contains fibroblasts and vascular cells, which can secrete cell growth factors to attract autologous cells to migrate to the wound, thus accelerating the healing process. Additionally, the upper epidermal structure can enhance the recruitment of autologous epidermal cells, effectively promoting epidermal regeneration. Wei *et al.*[52] developed miR-17-5p-engineered small extracellular vesicles (sEVs17-OE) and encapsulated them in GelMA hydrogel for treating diabetic wounds. Gel-sEVs17-OE effectively accelerated wound healing by promoting angiogenesis and collagen deposition. Cytokeratin 10 (CK10), a type I keratin and intermediate filament protein, is involved in the keratinization process of the skin, helping to maintain skin integrity and barrier function. Its expression level reflects the degree of keratinocyte differentiation. By Day 21, all three groups exhibited "ridge" structures in the epidermis, but there were differences in thickness. The epidermal thickness in the VS group was significantly greater than that in the other two groups, and the expression of IVL and CK10 in the VS group was higher than that in the other two groups, indicating that the epidermal reconstruction in the VS group was superior. This might be due to the VS group's faster healing speed and earlier entry into the epidermal-reconstruction stage. In addition, the vascularized dermal skin substitute contains an epidermal layer. The epidermal cells of the layer perform biological functions such as extracellular matrix secretion in the early healing stage, resulting in a better-matured healed epidermal layer. The CD31 fluorescence intensity and maximum vascular aperture in the VS group were higher than those in the other two groups. This may be because the cells in the vascularized dermal skin substitute continuously secrete cytokines and extracellular matrix during the healing process, accelerating the onset of biological functions and promoting the vascularization process of the newly-formed skin (Figure 8C). Zhang *et al.*[53] investigated using GelMA-HAMA-fibrin as a scaffold material, with human keratinocytes, fibroblasts, and umbilical vein endothelial cells as seed cells. They conducted a full-thickness skin wound healing experiment in a nude mouse model, and the results demonstrated that the printed organoid hydrogel significantly accelerated wound closure rates and improved epithelial regeneration in the nude mice.

3.8. Validation of printed vascularized skin substitutes in rabbits

Previous studies have shown that GelMA hydrogel positively affects the repair of full-thickness skin defects in rabbits.[54-56] The process of skin injury repair in New Zealand rabbits is illustrated in Figure 9A. The healing progress of the wounds was regularly photographed and recorded, and ImageJ was used to quantitatively measure the wound healing rate (Figure 9B). By Day 28, all groups except the untreated group had completely healed. By Day 21, the EK group had fully healed, while the untreated group (control), GelMA (Blank) group, and E group had healing rates of 96.43 ± 0.71%, 98.16 ± 0.46%, and 99.48 ± 0.38%, respectively. The VS and bilayer skin groups showed significantly higher healing rates than the other groups, indicating faster healing speeds. On Day 28, H & E staining was performed on the newly formed skin tissue and the host's native skin tissue (Figure 9C). The EK group showed significantly superior results compared to the other groups. The epidermal layer had developed a "ridge"-like structure and papillae, which were tightly integrated with the dermal layer. Additionally, melanocyte-like cells were observed in the basal layer. The E group also exhibited a "ridge"-like

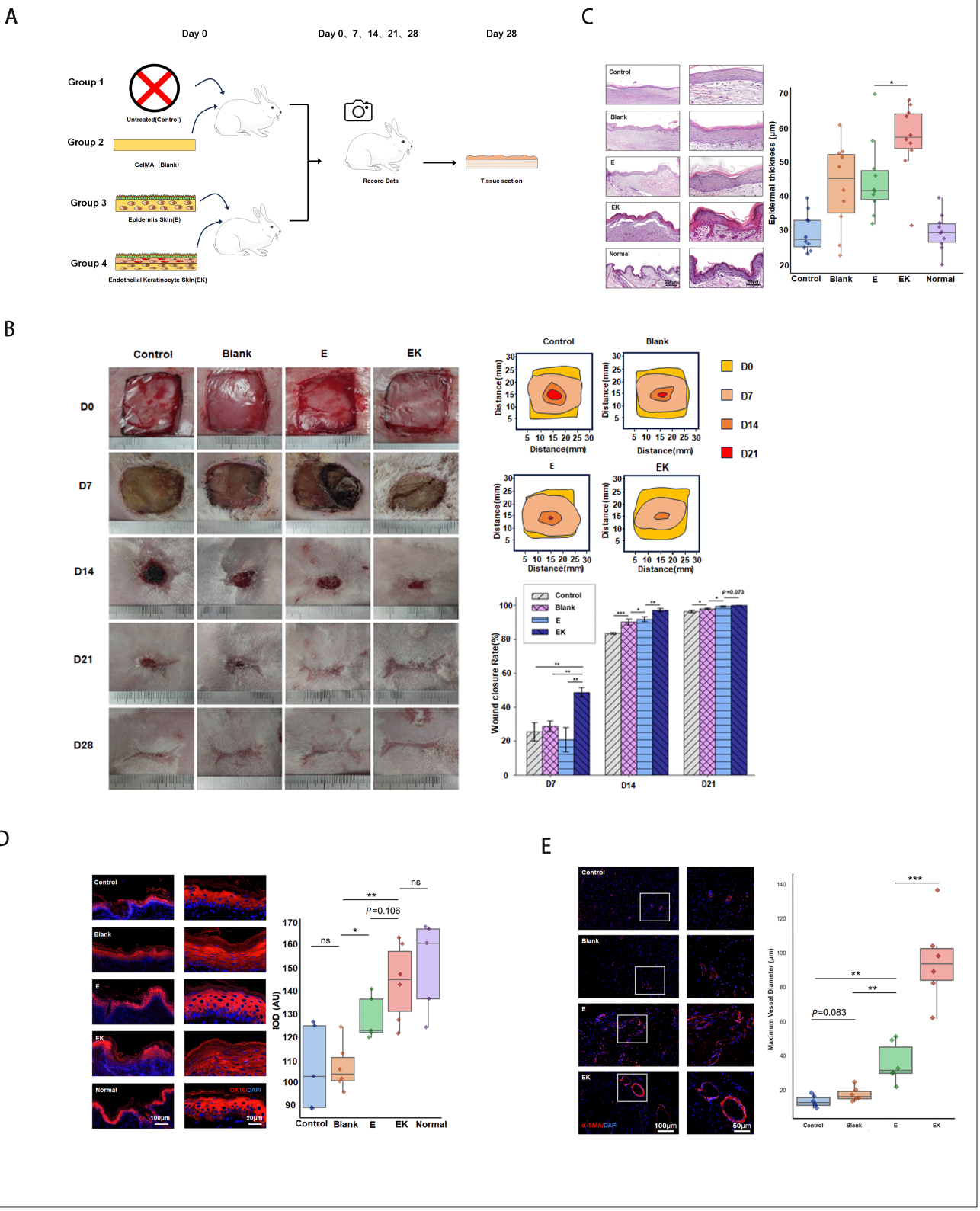
A
Day 0
Day 0、7、14、21、28
Day 28
Group 1
Untreated(Control)
Group 2
GelMA（Blank）
Group 3
Epidermis Skin(E)
Group 4
Endothelial Keratinocyte Skin(EK)
Record Data
Tissue section
C
Control
Blank
E
EK
Normal
Epidermal thickness (μm)
B
Control
Blank
E
EK
D0
D7
D14
D21
D28
Distance(mm)
Wound closure Rate(%)
P=0.073
D
CK10/DAPI
100μm
20μm
IOD (AU)
P=0.106
ns
E
α-SMA/DAPI
50μm
Maximum Vessel Diameter (μm)
P=0.083

Figure 9. Repair of dorsal skin defects in New Zealand rabbits. (A) Flowchart of the dorsal skin defect repair experiment in New Zealand rabbits. (B) Photographs of dorsal skin defect healing in New Zealand rabbits at Day 0, Day 7, Day 14, Day 21, and Day 28. By Day 28, all groups except the control group had completely healed. At Day 21, the endothelial keratinocyte skin (EK) group had already achieved complete healing, showing significant differences compared to the control group (96.43 ± 0.71%), blank group (98.16 ± 0.46%), and epidermis skin (E) group (99.48 ± 0.38%). (C) Hematoxylin and eosin staining revealed that the EK and E groups had developed a "ridge-like" structure in the epidermis. However, the dermo-epidermal junction in the E group was less defined compared to the EK group. The epidermal thickness in the EK group (56.59 ± 10.68 μm) was significantly greater than that in the E group (45.65 ± 13.81 μm). Scale bars: 50 and 200 μm; magnification: 200× and 40×. (D) Cytokeratin 10 (CK10) protein expression in the newly formed epidermis of New Zealand rabbits. The EK group showed significantly higher CK10 expression than the control and blank groups, but no significant difference was observed compared to the E group. Scale bars: 20 and 100 μm. (E) Alpha-smooth muscle actin protein expression in small blood vessels and measurement of the maximum vascular diameter in the newly formed skin of New Zealand rabbits. The EK group exhibited the largest vascular diameter (95.36 ± 24.87 μm), which was significantly different compared to the control group (13.53 ± 3.32 μm), blank group (17.69 ± 4.13 μm), and E group (35.83 ± 11.70 μm). Scale bars: 50 and 100 μm. Data were analyzed via a one-way analysis of variance and are shown as mean ± standard deviation (*$p < 0.05$, **$p < 0.01$, and ***$p < 0.001$, $n = 3$). Abbreviation: IOD, integrated optical density.

structure, but its integration with the dermal layer was less robust than that of the EK group. Tissue sections were subjected to CK10 staining (Figure 9D). The expression levels of CK10 in the EK and E groups were significantly higher than those in the other experimental groups. Specifically, the EK group (143.84 ± 8.55) showed a slightly higher expression level than the E group (128.30 ± 4.83). This indicates a higher degree of epidermal differentiation in these two groups, possibly due to the presence of epidermal cells. In contrast, the EK group has a more mature epidermal structure due to its accelerated early repair and longer epidermal generation time than the double-layer skin group. Moreover, it had more vascular cells/structures for oxygen supply for epidermal cell generation, resulting in a more mature epidermal structure. Alpha-smooth muscle actin (α-SMA) is mainly expressed in smooth muscle cells of the middle layer of blood vessels. In this experiment, α-SMA was selected as a marker for vascular characterization (Figure 9E), labeling newly formed small blood vessels in the subcutaneous tissue. The maximum vascular diameters for each group were as follows: control group (13.53 ± 3.32 μm), Blank group (17.69 ± 4.13 μm), E group (35.83 ± 11.70 μm), and EK group (95.36 ± 24.87 μm). It can be seen that the EK group, which contained vascular endothelial cells, had a much stronger ability for blood vessel regeneration than the other three groups. The double-layer skin group also had a higher blood vessel regeneration ability than the first two experimental samples because its repair speed was faster than the other two groups, and it contained fibroblasts, which could secrete VEGF and other factors that promote vascular cell formation. In summary, the 28-day experiment on back skin defects of New Zealand rabbits fully demonstrated that both the double-layer and VS substitutes were effective in repairing skin defects. Compared with the former, the latter showed improvements in promoting rapid wound healing, epidermal differentiation and shaping, and blood vessel neogenesis. Future studies must incorporate positive control groups (e.g., commercial collagen-based skin substitutes or autografts) and extend the experimental duration to provide more comprehensive insights.

4. Conclusion

This study successfully developed a method for constructing a 3D bioprinted VS substitute. By proposing a single-component hydrogel-cell-compatible composite ink, a GelMA hydrogel-cell-compatible ink targeting fibroblasts, keratinocytes, and vascular endothelial cells was formulated. Based on this, a gradient vascularization dermal skin substitute containing a reticular layer, a papillary layer, and an epidermal layer was gradually constructed. The 3D-printed VS was implanted into *BALB/c* nude mice and New Zealand rabbit skin defect models, validating the effectiveness of the VS substitute in promoting skin healing and angiogenesis. The VS substitute constructed by 3D bioprinting provides a promising strategy for treating skin injuries.

Acknowledgments

The authors thank Zhejiang University for providing the experimental equipment.

Funding

This work was supported by the National Key Research and Development Program of China (Grant No. 2018YFA0703000) and the Key Science and Technology Program of Zhejiang Province (Grant No. 2023C03170 and 2023C03071).

Conflict of interest

The authors declare no conflict of interest.

Author contributions

Conceptualization: Yichen Luo, Bin Zhang, Jien Ma
Data curation: Yichen Luo, Dan Li, Bin Zhang
Figure and visualization: Yichen Luo, Dan Li
Formal analysis: Yichen Luo

Investigation and resources: Yichen Luo,
Methodology and software: Yichen Luo, Cai Lin, Xue Zhou
Project administration and funding acquisition: Bin Zhang
Supervision: Bin Zhang, Jien Ma
Validation: Yichen Luo, Dan Li, Cai Lin, Xue Zhou
Writing – original draft: Yichen Luo, Dan Li
Writing – review & editing: Yichen Luo, Bin Zhang
All authors have read and agreed to the published version of the manuscript.

Ethics approval and consent to participate

The Institutional Animal Care and Use Committee of Zhejiang University approved the design of this study (Approval number: 31324 and 31325).

Consent for publication

Not applicable.

Availability of data

The data that support the findings of this study are available on request from the corresponding author. Additional method descriptions can be found in the supplementary method**.**

References

1. Lee SG, Lee S, Bae HK, et al. Evaluation of the therapeutic efficacy of human skin equivalents manufactured through droplet-based bioprinting/nebulization technology. *Mol cell Toxicol*. 2024;20(1):129-138.
doi: 10.1007/s13273-023-00330-9

2. Michael S, Sorg H, Peck CT, et al. Tissue engineered skin substitutes created by laser-assisted bioprinting form skin-like structures in the dorsal skin fold chamber in mice. *PLoS ONE*. 2013;8(3):e57741.
doi: 10.1371/journal.pone.0057741

3. Kafrashian Z, Brück S, Rogin P, et al. Segmented, side-emitting hydrogel optical fibers for multimaterial extrusion printing. *Adv Mater*. 2025;37(4): e2309166.
doi: 10.1002/adma.202309166

4. Lin Z, Qiu X, Cai Z, et al. High internal phase emulsions gel ink for direct-ink-writing 3D printing of liquid metal. *Nat Commun*. 2024;15(1):4806.
doi: 10.1038/s41467-024-48906-w

5. Zhang C, Hua W, Mitchell K, Jin Y. Multiscale embedded printing of engineered human tissue and organ equivalents. *Proc Natl Acad Sci USA*. 2024;121(9): e2313464121.
doi: 10.1073/pnas.2313464121

6. Sobreiro-Almeida R, Santos SC, Decarli MC, et al. Leveraging blood components for 3D printing applications through programmable ink engineering approaches. *Adv Sci*. 2024;11(47):2406569.
doi: 10.1002/advs.202406569

7. Dong T, Hu J, Dong Y, et al. Advanced biomedical and electronic dual-function skin patch created through microfluidic-regulated 3D bioprinting. *Bioact Mater*. 2024;40: 261-274.
doi: 10.1016/j.bioactmat.2024.06.015

8. Bebiano LB, Presa R, Vieira F, Lourenco BN, Pereira RF. Bioinspired and photo-clickable thiol-ene bioinks for the extrusion bioprinting of mechanically tunable 3D skin models. *Biomimetics (Basel)*. 2024;9(4):228.
doi: 10.3390/biomimetics9040228

9. Gu Z, Fu J, Lin H, He Y. Development of 3D bioprinting: from printing methods to biomedical applications. *Asian J Pharm Sci*. 2020;15(5): 529-557.
doi: 10.1016/j.ajps.2019.11.003

10. Selvam SP, Ayyappan S, Jamir SI, Sellappan LK, Manoharan S. Recent advancements of hydroxyapatite and polyethylene glycol (PEG) composites for tissue engineering applications–a comprehensive review. *Eur Polym J*. 2024;215: 113226.
doi: 10.1016/j.eurpolymj.2024.113226

11. Taite LJ, Rowland ML, Ruffino KA, Smith BRE, Lawrence MB, West J L. Bioactive hydrogel substrates: probing leukocyte receptor–ligand interactions in parallel plate flow chamber studies. *Ann Biomed Eng*. 2006;34: 1705-1711.
doi: 10.1007/s10439-006-9173-x

12. Coudane J, Nottelet B, Mouton J, Garric X, Berghe HVD. Poly (ε-caprolactone)-based graft copolymers: synthesis methods and applications in the biomedical field: a review. *Molecules*. 2022;27(21):7339.
doi: 10.3390/molecules27217339

13. Milosevic M, Stojanovic DB, Simic V, et al. Preparation and modeling of three-layered PCL/PLGA/PCL fibrous scaffolds for prolonged drug release. *Sci Rep*. 2020;10(1):11126.
doi: 10.1038/s41598-020-68117-9

14. Chen Y, Li J, Lu J, Ding M, Chen Y. Synthesis and properties of Poly (vinyl alcohol) hydrogels with high strength and toughness. *Polym Test*. 2022;108:107516.
doi: 10.1016/j.polymertesting.2022.107516

15. Zhao X, Lang Q, Yildirimer L, et al. Photocrosslinkable gelatin hydrogel for epidermal tissue engineering. *Adv Health Mater*. 2016;5(1):108-118.
doi: 10.1002/adhm.201500005

16. Xu W, Molino BZ, Cheng F, et al. On low-concentration inks formulated by nanocellulose assisted with gelatin methacrylate (GelMA) for 3D printing toward wound healing application. *ACS Appl Mater Interfaces*. 2019;11(9):8838-8848.
doi: 10.1021/acsami.8b21268

17. Mazio C, Casale C, Imparato G, et al. Pre-vascularized dermis model for fast and functional anastomosis with host vasculature. *Biomaterials*. 2019;192:159-170. doi: 10.1016/j.biomaterials.2018.11.018

18. Xu H, Liu Z, Wei Y, et al. Complexation-induced resolution enhancement pleiotropic small diameter vascular constructs with superior antibacterial and angiogenesis properties. *Adv Healthc Mater*. 2023;12(29):2301809. doi: 10.1002/adhm.202301809

19. Wan H, Cao Y, Lo LW, Zhao J, Sepúlveda N, Wang C. Flexible carbon nanotube synaptic transistor for neurological electronic skin applications. *ACS Nano*. 2020;14(8):10402-10412. doi: 10.1021/acsnano.0c04259

20. Vidal SEL, Tamamoto KA, Nguyen H, Abbott RD, Cairns DM, Kaplan DL. 3D biomaterial matrix to support long term, full thickness, immuno-competent human skin equivalents with nervous system components. *Biomaterials*. 2019;198:194-203. doi: 10.1016/j.biomaterials.2018.04.044

21. Xiong M, Yang X, Shi Z, et al. Programmable artificial skins accomplish antiscar healing with multiple appendage regeneration. *Adv Mater*. 2024;36(50): 2407322. doi: 10.1002/adma.202407322

22. Xia Y, Yan S, Wei H, et al. Multifunctional porous bilayer artificial skin for enhanced wound healing. *ACS Appl Mater Interfaces*. 2024;16(27):34578-34590. doi: 10.1021/acsami.4c05074

23. Ma J, Qin C, Wu J, et al. 3D multicellular micropatterning biomaterials for hair regeneration and vascularization. *Mater Horiz*. 2023;10(9):3773-3784. doi: 10.1039/d3mh00528c

24. Motter Catarino C, Cigaran Schuck D, Dechiario L, Karande P. Incorporation of hair follicles in 3D bioprinted models of human skin. *Sci Adv*. 2023;9(41):eadg0297. doi: 10.1126/sciadv.adg0297

25. Chen H, Ma X, Gao T, et al. Robot-assisted in situ bioprinting of gelatin methacrylate hydrogels with stem cells induces hair follicle-inclusive skin regeneration. *Biomed Pharmacother*. 2023;158:114140. doi: 10.1016/j.biopha.2022.114140

26. Zhao W, Chen H, Zhang Y, et al. Adaptive multi-degree-of-freedom in situ bioprinting robot for hair-follicle-inclusive skin repair: a preliminary study conducted in mice. *Bioeng Transl Med*. 2022;7(3):e10303. doi: 10.1002/btm2.10303

27. Dai LG, Dai NT, Chen TY, Kang LY, Hsu SH. A bioprinted vascularized skin substitute with fibroblasts, keratinocytes, and endothelial progenitor cells for skin wound healing. *Bioprinting*. 2022;28:e00237. doi: 10.1016/j.bprint.2022.e00237

28. Ma J, Qin C, Wu J, et al. 3D printing of strontium silicate microcylinder-containing multicellular biomaterial inks for vascularized skin regeneration. *Adv Healthc Mater*. 2021;10(16):2100523. doi: 10.1002/adhm.202100523

29. Barros NR, Kim HJ, Gouidie MJ, et al. Biofabrication of endothelial cell, dermal fibroblast, and multilayered keratinocyte layers for skin tissue engineering. *Biofabrication*. 2021;13(3):035030. doi: 10.1088/1758-5090/aba503

30. Xiang P, Yan L, Ge L, He X, Du N, Liu X. Development of a radial-flux machine with multi-shaped magnet rotor and non-ferromagnetic yoke for low torque ripple and rotor mass. *IEEE Trans Ind Appl*. 61;2025:2897-2910. doi: 10.1109/TIA.2025.3532558

31. Xiang P, Yan L, Guo Y, He X, Gerada C, Chen IM. A concentrated-flux-type pm machine with irregular magnets and iron poles. *IEEE/ASME Trans Mech*. 2023;29(1): 691-702. doi: 10.1109/TMECH.2023.3293505

32. Guo J, Gu H, Yin S, et al. Hepatocyte-derived Igκ promotes HCC progression by stabilizing electron transfer flavoprotein subunit α to facilitate fatty acid β-oxidation. *J Exp Clin Cancer Res*. 2024;43(1):280. doi: 10.1186/s13046-024-03203-8

33. Liu C, Qin W, Wang Y, et al. 3D printed gelatin/sodium alginate hydrogel scaffolds doped with nano-attapulgite for bone tissue repair. *Int J Nanomed*. 2021;16:8417-8432. doi: 10.2147/IJN.S339500

34. Pierce MC, Strasswimmer J, Hyle Park B, Cense B, De Boer JF. Birefringence measurements in human skin using polarization-sensitive optical coherence tomography. *J Biomed Opt*. 2004;9(2):287-291. doi: 10.1117/1.1645797

35. Wang Y, Liu Y, Chen S, et al. Enhancing bone regeneration through 3D printed biphasic calcium phosphate scaffolds featuring graded pore sizes. *Bioact Mater*. 2024;46:21–36. doi: 10.1016/j.bioactmat.2024.11.024

36. Kim BS, Yang WK, Jeong SK, et al. 3D cell printing of in vitro stabilized skin model and in vivo pre-vascularized skin patch using tissue-specific extracellular matrix bioink: a step towards advanced skin tissue engineering. *Biomaterials*. 2018;168:38-53. doi: 10.1016/j.biomaterials.2018.03.040

37. Won-woo C, Minjun A, Byoung SK, Dong-Woo C. Blood-lymphatic integrated system with heterogeneous melanoma spheroids via in-bath three-dimensional bioprinting for modelling of combinational targeted therapy. *Adv Sci*. 2022;9(29):2202093. doi: 10.1002/advs.202202093

38. Song J, Liu T, Liao Z, et al. Digital light processing bioprinting neural systems with porous hydrogel in structure and function for disease models. *Cell Rep Phys Sci*. 2024;5(12):102311. doi: 10.1016/j.xcrp.2024.102311

39. Zandi N, Daniele M, Brown A. Advances in fibrin-based bioprinting for skin tissue regeneration: exploring design, and innovative approaches. *Biomed Mater Devices*. 2025;3:330-348.
doi: 10.1007/s44174-024-00198-w

40. Fauzi MB, Rashidbenam Z, Bin Saim A, Binti Hj Idrus R. Preliminary study of in vitro three-dimensional skin model using an ovine collagen type i sponge seeded with co-culture skin cells: submerged versus air-liquid interface conditions. *Polymers*. 2020;12(12): 2784.
doi: 10.3390/polym12122784

41. Monsuur HN, Boink MA, Weijers EM, et al. Methods to study differences in cell mobility during skin wound healing in vitro. *J Biomech*. 2016;49(8):1381-1387.
doi: 10.1016/j.jbiomech.2016.01.040

42. Petry L, Kippenberger S, Meissner M, et al. Directing adipose-derived stem cells into keratinocyte-like cells: impact of medium composition and culture condition. *J Eur Acad Dermatol Venereol*. 2018;32(11):2010-2019.
doi: 10.1111/jdv.15010

43. Colin E, Plyer A, Golzio M, Meyer N, Faver G, Orlik X. Imaging of the skin microvascularization using spatially depolarized dynamic speckle. *J Biomed Opt*. 2022;27(4):046003.
doi: 10.1117/1.Jbo.27.4.046003

44. Hu X, Wang L, Deng J, et al. Dietary nitrate accelerates the healing of infected skin wounds in mice by increasing microvascular density. *Biochem Biophys Res Commun*. 2023;686:149176.
doi: 10.1016/j.bbrc.2023.149176

45. Fu T, Sullivan DP, Gonzalez AM, et al. Mechanotransduction via endothelial adhesion molecule CD31 initiates transmigration and reveals a role for VEGFR2 in diapedesis. *Immunity*. 2023;56(10):2311-2324.e6.
doi: 10.1016/j.immuni.2023.08.001

46. Park H, Collignon AM, Lepry WC, et al. Acellular dense collagen-S53P4 bioactive glass hybrid gel scaffolds form more bone than stem cell delivered constructs. *Mater Sci Eng C Mater Biol Appl*. 2021;120:111743.
doi: 10.1016/j.msec.2020.111743

47. Trappmann B, Gautrot JE, Connelly JT, et al. Extracellular-matrix tethering regulates stem-cell fate. *Nat Mater*. 2012;11(7): 642-649.
doi: 10.1038/nmat3339

48. Singh A, Dalal N, Tayalia P. An interplay of matrix stiffness, dimensionality and adhesivity on cellular behavior. *Biomed Mater*. 2023;18(2): 025010.
doi: 10.1088/1748-605X/acb7c0

49. Trujillo S, Gonzalez-Garcia C, Rico P, et al. Engineered 3D hydrogels with full-length fibronectin that sequester and present growth factors. *Biomaterials*. 2020; 252:120104.
doi: 10.1016/j.biomaterials.2020.120104

50. Ito M, Hiramatsu H, Kobayashi K, et al. NOD/SCID/γ c null mouse: an excellent recipient mouse model for engraftment of human cells. *Blood*. 2002;100(9):3175-3182.
doi: 10.1182/blood-2001-12-0207

51. Albanna M, Binder KW, Murphy SV, et al. In situ bioprinting of autologous skin cells accelerates wound healing of extensive excisional full-thickness wounds. *Sci Rep*. 2019;9(1):1856.
doi: 10.1038/s41598-018-38366-w

52. Wei Q, Su J, Meng S, et al. MiR-17-5p-engineered sEVs encapsulated in GelMA hydrogel facilitated diabetic wound healing by targeting PTEN and p21. *Adv Sci (Weinh)*. 2024;11(13):2307761.
doi: 10.1002/advs.202307761

53. Zhang G, Zhang Z, Cao G, et al. Engineered dermis loaded with confining forces promotes full-thickness wound healing by enhancing vascularisation and epithelialisation. *Acta Biomater*. 2023; 170: 464-478.
doi: 10.1016/j.actbio.2023.08.049

54. Jin T, Fu Z, Zhou L, et al. GelMA loaded with platelet lysate promotes skin regeneration and angiogenesis in pressure ulcers by activating STAT3. *Sci Rep*. 2024; 14(1): 18345.
doi: 10.1038/s41598-024-67304-2

55. Chen L, Ye JL, Gao C, Deng F, Liu W, Zhang Q. Design and fabrication of gelatin-based hydrogel loaded with modified amniotic extracellular matrix for enhanced wound healing. *Heliyon*. 2023;9(10):e20521.
doi: 10.1016/j.heliyon.2023.e20521

56. Hao X, Luo J, Huang Y, et al. Injectable antiswelling and high-strength bioactive hydrogels with a wet adhesion and rapid gelling process to promote sutureless wound closure and scar-free repair of infectious wounds. *ACS Nano*. 2023;17(21): 22015-22034.
doi: 10.1021/acsnano.3c08625